BRUNEL UNIVERSITY

Signal Processing Methods for Defect Detection in Multi-Wire Helical Waveguides using Ultrasonic Guided Waves

by

Mehmet Kerim Yucel

A thesis submitted in partial fulfillment for the

degree of Master of Philosophy

in the

School of Engineering and Design

March 2015

ABSTRACT

Non-Destructive Testing of industrial components carries vital importance, both financially and safety-wise. Among all Non-Destructive techniques, Long Range Ultrasonic Testing utilizing the guided wave phenomena is a young technology proven to be commercially valid. Owing to its well-documented analytical models, Ultrasonic Guided Waves has been successfully applied to cylindrical and plate-like structures. Its applications to complex structures such as multi-wire cables are fairly immature, mainly due to the high complexity of wave propagation.

Research performed by the author approaches the long range inspection of overhead transmission line cables using ultrasonic guided waves. Existing studies focusing on guided wave application on power cables are extremely limited in inspection range, which dramatically degrades its chances of commercialization. This thesis consists of three main chapters, all of which approaches different problems associated with the inspection of power cables.

In the first chapter, a thorough analysis of wave propagation in ACSR (most widely used power cable) cables is conducted. It is shown that high frequency guided waves, by concentrating the energy on the surface layers, can travel much further in the form of fundamental longitudinal wave mode, than previous studies have shown. Defect detection studies proved the system's capability of detecting defects which introduce either increase or decrease in cross sectional area of the cable. Results of the chapter indicate the detectability of defects as small as 4.5% of the cross sectional area through a 26.5 meter long cable without any post-processing.

In the second chapter, several algorithms are proposed to increase the inspection range and signal quality. Well-documented wavelet-denoising algorithm is optimized for power cables and up to 24% signal-to-noise ratio improvement is achieved. By introducing an attenuation correction framework, a theoretical inspection range of 75 meters is presented. A new framework combining dispersion compensation and attenuation correction is proposed and verified, which shows an inspection range of 130 meters and SNR improvement up to 8 dBs.

Last chapter addresses the accurate localization of structural defects. Having proven the optimum excitation and related wave propagation in ACSR cables, a system having a more complex wave propagation characteristics is studied. A new algorithm combining pulse compression using Maximal Length Sequences and dispersion compensation is applied to multi-modal signals obtained from a solid aluminum rod. The algorithm proved to be able to improve signal quality and extract an accurate location for defects. Maximal Length Sequences are compared to chirp signals in terms of SNR improvement and localization, which produced favourable results for MLS in terms of localization and for chirp in terms of SNR improvement.

ACKNOWLEDGEMENTS

The author thanks the personnel of Brunel Innovation Centre and TWI who have provided continuous support to the author throughout his research. Support of Dr.Alvin Chong, Dr. Hossein Habibi, Dr.Abbas Mohimi, Maria Kogia, Sina Fateri, Shehan Lowe and Dr. Cem Selcuk is gratefully acknowledged and will never be forgotten.

The work presented in this thesis could not have been completed without the technical and emotional support of Dr. Makis Livadas and Vassilios Tzitzilonis. Author also extends his eternal gratitude to Dr. Mathew Legg, in addition to his immense support and sublime supervision, who simply made this research and thesis happen. Author would like to thank Prof. Abdul Sadka and Prof. Tat-Hean Gan of Brunel University to realize the opportunity of this research in the first place. A special thanks goes to Dr. Vassilis Kappatos, who have willingly (or unwillingly, the author is not entirely sure) and successfully managed to endure author's frequent emotional fluctuations and unending problems, be it technical or financial.

The author will eternally remain grateful to Prof. Wamadeva Balachandran due to his continuous technical and emotional support. His mentorship and invaluable feedbacks regarding every possible question was the main factor that held this research together.

Last but foremost, author acknowledges the endless support of family and friends in Turkey and UK who have helped the author maintain his focus and motivation to pursue this research.

The author gratefully acknowledges European Commission, TSB and Brunel University, without whom the research would have been impossible.

With the hopes of seeing again the people listed above somehow, somewhere, sometime.

Babam için

TABLE OF CONTENTS

LIST OF FIGURES

LIST OF TABLES

LIST OF ABBREVIATIONS

NDT	*Non-Destructive Testing*
RT	*Radiography Testing*
AE	*Acoustic Emission*
ECT	*Eddy Current Testing*
SEM	*Scanning Electron Microscopy*
MPI	*Magnetic Particle Inspection*
MFL	*Magnetic Flux Leakage*
ACFM	*Alternating Current Field Measurement*
UGW	*Ultrasonic Guided Waves*
OVTL	*Overhead Transmission Line*
ACSR	*Aluminum Conductor Steel Reinforced*
PZT	*Lead Zirconium Titanate*
LSV	*Laser Scanning Vibrometry*
CSA	*Cross Sectional Area*
STFT	*Short Time Fourier Transform*
LRUT	*Long Range Ultrasonic Testing*
SNR	*Signal to Noise Ratio*
RMS	*Root Mean Square*
DWT	*Discrete Wavelet Transform*
WFT	*Warped Frequency Transform*
PuC	*Pulse Compression*
ToF	*Time of Flight*
WDR	*Wideband Dispersion Reversal*
AWGN	*Additive White Gaussian Noise*
TCG	*Time Corrected Gain*
MLS	*Maximal Length Sequences*
LFSR	*Linear Feedback Shift Register*

LIST OF NOMENCLATURE

$\mathbf{H}$	*Curl of a vector potential*
$\boldsymbol{\varphi}$	*Sum of a scalar compressional gradient*
$\mathbf{C_l}$, $\mathbf{C_s}$, $\mathbf{C_s}$	*Longitudinal, shear and Rayleigh wave velocity*
$\boldsymbol{\rho}$	*Material density*
$\boldsymbol{\mu}$,$\boldsymbol{\lambda}$	*Lamé* constants; dynamic viscosity and first parameter
$\mathbf{A_l}$, $\mathbf{A_s}$	*Longitudinal and shear wave amplitude*
$\mathbf{k_l}$, $\mathbf{k_s}$	*Longitudinal and shear wavenumber*
$\mathbf{E}$	*Young's Modulus*
$\mathbb{\Gamma}$	*Coordinate variation (in spherical system)*
$\boldsymbol{u}$	*Displacement fields (in spherical system)*
$\boldsymbol{\omega}$	*Angular frequency*
$\boldsymbol{\sigma}$	*Standard deviation*
$\boldsymbol{\alpha}$	*Positive constant for attenuation correction*
$\boldsymbol{IFFT}$	*Inverse Fourier Transform operation*
$\boldsymbol{ccf}$	*Cross correlation operation*
$\boldsymbol{\delta}$	*Dirac-delta function*
$\mathbf{V_{gr}}$, $\mathbf{V_{ph}}$	*Group and phase velocity ($\boldsymbol{C_{gr}}$, $\boldsymbol{C_{ph}}$)*
$\mathbf{L_{Helical}}$	*Helical Length*

CHAPTER 1: Research Background and Motivation

1.1. :Overview

This short chapter serves as an executive summary to give the readers an overview of the research reported in this thesis along with a summary of the methodology, brief information about the research background, aims of the research, an organization of the entire thesis and the novelties arising from this thesis, many of which are submitted to scientific journals and conferences.

1.2. :Non-Destructive Testing and Ultrasonic Guided Waves

Non-Destructive Testing (NDT) techniques are extensively used in numerous branches of industry to monitor the integrity of industrial components for two main reasons; meeting the health and safety criteria for the personnel and to stay informed about the health of the components to keep monetary consequences under control. NDT techniques based on various branches of science exist; from visual inspection to electromagnetic testing, x-rays, RF-noise control, infrared methods, ultrasonic and many more. As heavy industry is in dire need of efficient methods, academia stepped up to meet the demands and to further advance the existing methods for increased inspection quality and reduced cost, thus fueling the recent interest in NDT research.

Although ultrasonic testing has been widely used as an NDT technique for a long time, recent advances made in the last few decades opened a new frontier as a sub-branch of ultrasound in heavy industry; ultrasonic guided waves. Owing to its long range propagation capability, which in turn means reduced operational costs and opportunity of scanning long ranges from a single contact point, ultrasonic guided waves emerged as a valid and attractive field of research, both for industry and academia. Several industries, such as oil/gas, civil engineering and aviation have been injecting a lot of money, both for inspection and permanent monitoring purposes. Although its theory is well-documented for rather simple structures and its associated software tools for engineering purposes have reached a certain level of maturity, there are still unexplored areas of ultrasonic guided waves research as the wave propagation characteristics is highly dependent on the structure of interest. Moreover, there are still problems that guided wave applications inherited from its physical properties, such as detectability of small defects, closely spaced defects, detecting defects under noisy conditions, accurate localization of defects and limited inspection range. When afore mentioned problems are coupled with the highly complex problem of wave propagation modeling in complex structures, one can see the complexity of the problem increases dramatically.

1.3. :Research Motivation

As the existing power line cable network is reaching a considerable age, there is a huge need for inspection of power line cables. Moreover, the hostile operating conditions that the power line cables

are working in means that cables are prone to errors. Considering that power line cables are the only means to transport power between long distances and the ever increasing energy consumption in the world, the problem of inspection power line cables is an attractive problem both for industry and academia. There are various existing methods applied for NDT of power line cables, such as helicopter assisted visual inspection, eddy current based inspection, radio frequency noise monitoring, fiber optic monitoring, robotics-powered systems and infrared systems. However, those systems still have inherent drawbacks either in terms of cost, applicability or inspection range. There have been attempts by the academia to investigate ultrasonic guided waves for power line cables, but it has proved itself to be a highly complex problem due to cables' non-linear structure (i.e. inter-wire contact) and the hardship of obtaining an analytical solution, or lack thereof. Existing applications are also extremely limited in inspection range, lowering the chances of monetization and also leaving a gap in the scientific literature.

1.4. :Aims and Objectives

Inspired by the problems outlined in the previous part, this research attempts to further investigate guided wave propagation in power line cables and to advance the state of the art with an emphasis on industrial applicability of the guided wave technology. The specific objectives of this research are outlined below.

- To investigate the wave propagation in power line cables in-depth using theoretical analysis and extensive experimental work.
- To optimize guided wave propagation to increase inspection range for power line cables from one single contact point.
- To develop or implement existing signal processing methods to further increase inspection range.
- To develop or implement existing signal processing methods to increase captured signal quality.
- To develop or implement existing signal processing methods to accurately and automatically localize structural discontinuities, thus lowering the operational requirements.

1.5. :Summary of the Methodology and Organisation of the Thesis

In this thesis, the problem of UGW based inspection of OVTL cables is approached with an emphasis on experimentation. Therefore, the methodology adopted in this thesis starts with experimentation and then required comparisons and derivations are made using analytical or numerical models. As visualized in Figure I-1, a wide data base of signals is created through intensive experimentation on ACSR cables spanning various defect scenarios. This is followed by post-processing chapters which cover various techniques, either developed from scratch or adopted/optimized from existing literature, to address various problems of UGW based NDT systems.

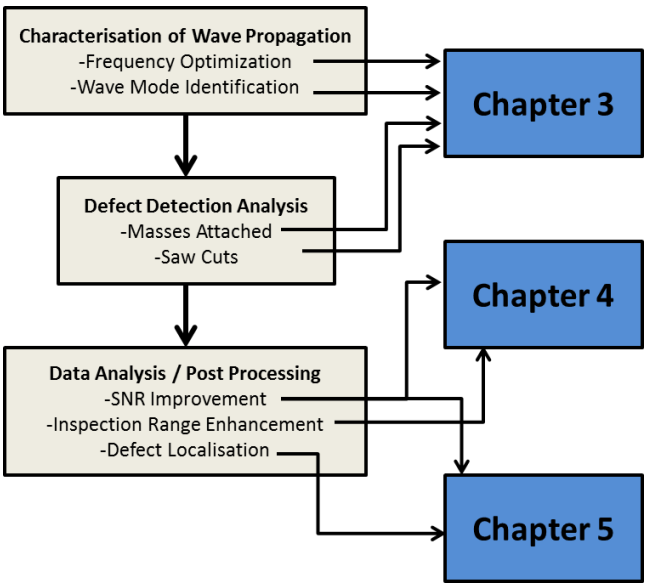

Figure 1-1 Diagram representing the methodology adopted in this thesis. Each step of the methodology is connected to its respective chapters where they are explained. Please note some tasks are connected to multiple chapters, meaning that the same goal is approached using different techniques/algorithms.

The content of this research is presented in three main chapters, all of which attack the problem of inspection of power line cables from various perspectives. Firstly, a thorough introductory chapter is presented (Chapter 1) which provides the readers with the necessary state-of-the-art information about NDT techniques, the analytical models of UGW and important concepts such as wave modes and dispersion. Following this introduction, thesis closely follows the methodology presented above. The problems are listed as the characterization and optimization of wave propagation for increased range of inspection for power line cables via thorough experimentation(Chapter 3), analysis and development of signal processing methods for signal quality improvement and inspection range enhancement (Chapter 4), and to automatically and accurately localize defects for all existing guided wave applications (Chapter 5). There are various aspects of this work which include novel approaches and contributions to knowledge. Next section of this chapter outlines the novelties.

1.6. :Contributions to Knowledge

The novelties reported in thesis are briefly outlined below in a chapter-by-chapter basis.

- **Chapter 3**
  - Through vibrometer and defect-detection analysis, a long cable (25 m) is successfully scanned for defects using a pulse-echo scheme (single contact point). *To the best of author's knowledge, this is the longest range achieved for a guided-wave based inspection of power line cables so far.* Defect corresponding to 4.5% decrease in cross sectional area of the cable is successfully detected. Frequency optimization studies indicate that by increasing the excitation frequency and concentrating the wave energy

to the outer wires of the cable (via skin effect), one can inspect long sections of power line cables. This result also has a significant merit in the sense that guided wave applications are generally low frequency (<100 kHz) since high frequency ultrasound is known to have a high attenuation constant. Moreover, it is seen that wave modes travelling through the cable are reminiscent that of a single wire case (wire forming the cable bundle).

- **Chapter 4**
  - Although the inspection of 25 metre long cable from a single contact point is appealing, further advances in inspection range is also desirable. As the associated limitations from a physics standpoint are rather hard to solve, a post-processing approach is adopted. The problem is broken into two parts in this chapter; improvement of SNR of the acquired signals and to increase the inspection range. Application of wavelet denoising techniques produced dramatic improvement of SNR (up to 24%). Adaptation of attenuation correction framework for power line cables also resulted into a theoretical tripling of the inspection range, reaching up to 75 meters. Lastly, as the high frequency guided waves tend to be dispersive, dispersion compensation techniques are combined with attenuation correction framework. Results indicate SNR improvement up to 8 dBs, and also approximately five-fold increase in inspection range, reaching up to 130 meters. This result dramatically improves the inspection range result obtained in the first chapter. *To the best of author's knowledge, this is the longest range achieved for a guided-wave based inspection of power line cables so far*. *Moreover, adaptation and optimization of wavelet denoising, attenuation correction and dispersion compensation haven't been reported in the literature for power line cables as of this moment.*
- **Chapter 5**
  - Focusing on another inherent problem of guided waves based systems in general; a new algorithm is developed to automatically locate the defect in the structure accurately whilst improving the SNR of the received signal, further increasing the chances of defect characterization. The proposed algorithm combines pulse compression based on Maximal Length Sequences/chirped sinusoids and dispersion compensation. The algorithm blindly compensates for dispersion the received signal assuming a random propagation distance using a priori knowledge of which wave mode is received and its group velocity dispersion curves. In every iteration, cross correlation between the received signal and the excited signal is taken, and its maximum value is stored. Once the above mentioned process is completed for a range of propagation distances, the stored maximums in the vector are analyzed and the maximum of this vector is found. This maximum vector corresponds to the propagation distance of the echo, thus the location of the defect. In addition to the novelty of the technique itself, MLS signals proved to produce better results than commonly used chirped sinusoids in terms of propagation distance extraction. Moreover, chirped sinusoids proved to be more useful in terms of SNR improvement. MLS and chirped signal are also analyzed for their performance under noisy conditions. *To the best of author's knowledge, such technique using MLS signals are being reported in the NDT literature for the first time.*

1.7. :Publications

Publications arising from the research reported in this thesis are listed below.

- **M.K. Yucel**, M. Legg, V. Kappatos, C. Selcuk, T.H. Gan, W. Balachandran "*An Ultrasonic Guided Wave approach for inspection of Overhead Transmission Line", under preparation for submission to a journal.*
- **M.K. Yucel**, S. Fateri, M.Legg, A. Wilkinson, V.Kappatos, C.Selcuk, T.H. Gan, "Pulse-Compression based Iterative Time-of-Flight Extraction of Dispersed Ultrasonic Guided Waves*",* submitted to INDIN IEEE International Conference on Industrial Informatics 2015.
- **M.K. Yucel**, M. Legg, M.Livadas , V. Kappatos, C. Selcuk, T.H. Gan, " *Identification and Utilisation of Ultrasonic Guided Waves for Inspection of ACSR Cables*", ECNDT' 2014 Conference, 2014.
- M. Legg, **M.K. Yucel**, V. Kappatos, C. Selcuk, T.H. Gan, "*Increased Range of Ultrasonic Guided Wave Testing of ACSR Cables using Dispersion Compensation*", Ultrasonics, 2014. (submitted, second round of reviews)

1.8. :Critical Summary

A brief summary of the thesis is presented in this chapter. Next chapter presents an in-depth literature review of Non-Destructive Testing, its brief history, commonly used techniques, detailed explanation of ultrasonic guided waves and important concepts associated with it.

CHAPTER 2: Introduction

2.1. :Overview

This chapter presents the necessary introductory information about the contributions reported in this thesis. Fundamentals of NDT, existing techniques along with their principles, areas of use and advantages/disadvantages are succeeded by sections on ultrasonic testing and ultrasonic guided waves, their respective analytical models and important concepts about UGW, such as guided wave modes in plate-like/cylindrical structures, dispersion problem and other inherent issues about guided wave applications of different nature.

2.2. :Non-Destructive Testing

2.2.1. :Fundamentals

Non-Destructive Testing , also known as Non-Destructive Evaluation and Non-Destructive Inspection, is defined as a group of interrogation techniques used in various branches of industry to assess materials and systems for their properties as well as their structural integrity. The importance of Non-Destructive Testing, compared to so-called *Destructive Techniques*, is that these techniques don't introduce permanent affects to the material or system of interest in any way, which basically means the integrity and the properties of the structure are preserved throughout the process. Moreover, many NDT techniques can be used while systems are active, thus saving the industrial parties both time and money **[1].**

As NDT techniques are commonly used in industry, their emergence can be related to the industrial revolution in the late 18^{th} century. Industrial revolution triggered a massive industrialization in the world, which means numerous factories created various jobs in environments with a high health and safety risk factor. Hazardous work environments lead to fatal accidents in many cases. One example is the explosion which took place in USA at a factory that left over 20 people dead and injured scores of people. In this case, fatal explosion triggered the enactment of laws enforcing periodic inspection of industrial systems of possible harm. Moreover, aside from the health hazards, deterioration of industrial systems due to simple aging and continuous use had a monetary impact on investors and employers, which raised the necessity of inspection of such systems on a periodic basis **[2]**.

Owing to its practicality and the high demand associated with its applications, researchers with different backgrounds have focused on developing NDT techniques. As a result, numerous NDT techniques utilizing different branches of science have emerged. Next section provides a brief overview of existing NDT techniques.

2.2.2. :Existing Techniques

In this section, underlying principles and associated applications of several NDT techniques are briefly explained in order to give the reader background information with regards to the field in general. If available, advantages and disadvantages of the respective techniques are also outlined.

2.2.2.1. :Radiography Testing

Industrial radiography technique utilizes the unique behavior of X-rays and gamma rays. By ionizing the radiation using x-ray and gamma rays, hidden flaws in structures can be accessed and detected. Owing to the discovery of X-rays, radiographic testing uses radioactive materials such as Iridium-192 in X-ray tomography systems. In contrast with the widely adopted photon-based radiography, neutron radiography is also used to penetrate materials of different properties. The basic idea behind radiographic testing is that the structural discontinuities would absorb more energy compared to the intact parts of the system. This energy absorption can then be imaged via data analysis and flaws can be found **[3]**. This technique is generally employed to inspect structural welds and pipe welds, many of which might include hidden flaws or flaws in inaccessible areas. Since the radiation could be measured from the other side of the interrogated material, material properties such as thickness could also be obtained via radiography testing.

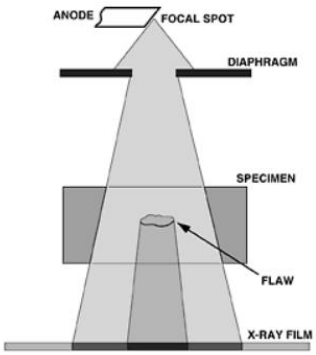

Figure 2-1 Schematic diagram of an example radiographic testing system. Image taken from [4].

As a non-contact method, RT can be useful; however its capital cost and the need of skilled operators might be seen as downsides of the method. Moreover, due to the use of radioactive materials, health risks are also present and fatal accidents have also been reported **[4, 5]**.

2.2.2.2. :Acoustic Emission

Acoustic emission is a technique which utilizes the phenomenon of energy release whenever a structural discontinuity is formed in the system. Release of strain energy propagates as transient acoustic waves, and this wave can be captured and analyzed for structural integrity analysis. Permanent installation of AE sensors enables passive monitoring, which is in contrast with many NDT techniques where systems are actively monitored. Passive monitoring is power-efficient and enables continuous monitoring of the system of interest. AE is also known to be efficient for material characterization purposes **[6]**.

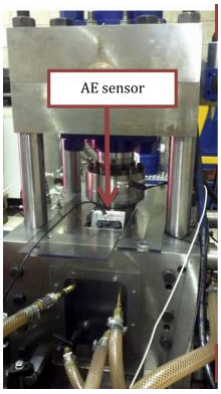

Figure 2-2 Acoustic emission applied to rotating machinery testing. Image taken from [7].

AE is employed in various fields such as bridges, refineries, offshore platforms, aircraft and rotating machinery **[8]**. Although it is perceived as a cost-effective technique for structural health monitoring, interpretation of AE signals is considered to be a difficult task since AE signals are generally complex. AE signals are generally observed to be in a wide frequency range (100 kHz – 1MHz) and the analysis of AE signals are performed via various signal processing and machine learning techniques **[9]**.

2.2.2.3. :Eddy Current Testing

Eddy current testing exploits the interaction between the interrogated specimen and electromagnetic induction generated by a coil. Whenever an AC current is fed to a coil, resulting magnetic field interacts with the system and creates eddy current on the material. When the generated eddy current is analyzed, either with the excitation coil or a second coil, the changes in amplitude and phase of the signal indicates the presence of a flaw. In addition to normal eddy current testing where single frequency components are used to drive the coil, pulsed eddy current techniques employ rectangular waves and thus allows multiple frequency excitation, which in theory includes rich information with regards to the flaw. Eddy current testing allows detection of both surface and subsurface flaws in the material. Moreover, no contact is required and material properties (i.e. thickness, conductivity) are reported to be measured accurately using eddy current testing **[10, 11]**.

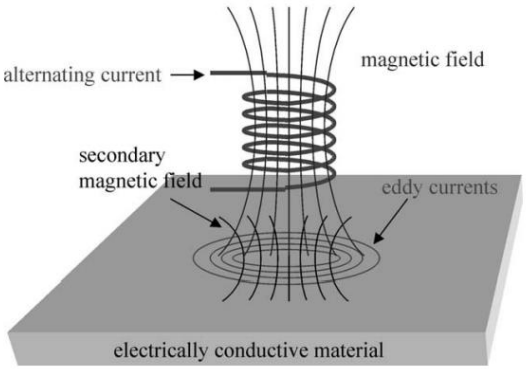

Figure 2-3 Explanatory diagram for eddy current testing principle. Image taken from [12].

Eddy current testing is used in many applications, such as aircrafts, pipes, metal structures and industrial refineries. A drawback of ECT is the limitation imposed by its physical nature; it can only be used for interrogating conductive materials **[13].**

2.2.2.4. :Scanning electron microscopy

Scanning electron microscopy uses electron beam guns to scan a surface of the test material via firing focused electron beams, either in a static or a swept manner. Electron beams interact with the atoms on the sample. Reflected and backscattered electrons, when received, produces a signal pattern which varies with respect to the material structure and surface topography. Signal patterns can then be imaged to yield structural integrity information of the sample **[14, 15]**.

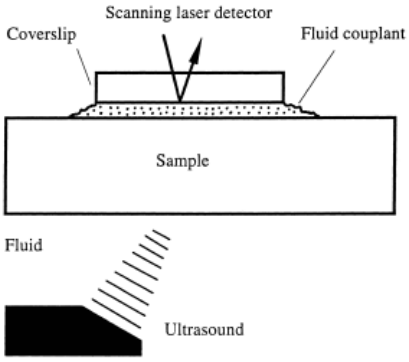

Figure 2-4 An example diagram for Scanning Acoustic Laser Microscopy. Image taken from [16].

SEM has been of interest for the NDT community due to its minimal preparation requirements. Moreover, high resolution imaging is also reported in various studies, enabling micro-scale inspection and atomic composition imaging. SEM is widely used to detect electrical failures in MEMS devices, integrated circuits, and for process control and quality assurance in the industry **[16]**.

2.2.2.5. :Infrared Thermography

Exploitation of temperature changes for NDT purposes is a commercially valid method of assessment of various structures. Although the way of capturing the thermal oscillations in the structure may vary, infrared thermography is one of the most common temperature based NDT techniques. Infrared thermography systems capture the thermal variations (thermal radiations with wavelengths ranging from 0.75 to 10 micrometer) in the structure via infrared sensors, mainly infrared cameras. The received radiation is reported to be a function of temperature and material emissivity. Therefore, once the received radiation is imaged to produce a heat map, information can be obtained about the structural integrity and the properties of the test material **[17]**.

IR thermography systems can work in either passive or active mode. The former arrangement makes use of the existing thermal contrast between the material and the surroundings whereas the latter generally uses an external stimulant (i.e. heat guns, heat lamps, etc…) to generate a thermal contrast in the system. There are various sub-branches of IR thermography such as pulsed thermography (PT), pulsed phase thermography and thermal modeling **[18]**.

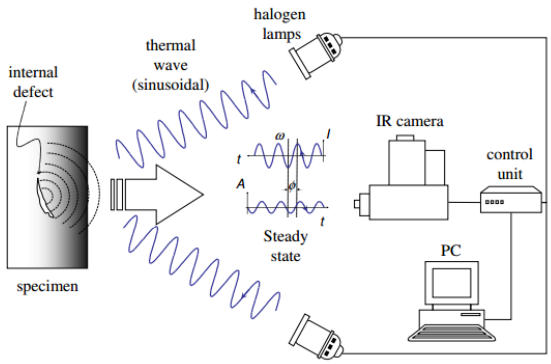

Figure 2-5 Experimental setup for lock-in thermography, a subset of IR thermography. Image taken from [19].

IR thermography is reported to have many advantages such as its speed, the range it might cover, the low temperature changes it can detect (i.e. the resolution) and the relatively low health risks since it is a non-contact method. The disadvantages associated with this technique are the limitation of material penetration and its sensitivity to weather/environment conditions. IR thermography technique is valid in various commercial applications such as pipes, honeycomb sandwich structures, bridges, assessment of electronic components and concrete structures **[20]**.

2.2.2.6. :Electromagnetic testing

Electromagnetic testing techniques introduce magnetic fields or electric currents to interrogate test systems and draws structural information about the test subject based on the response of the material. There are various electromagnetic testing techniques specializing in different applications and systems. Such techniques include, but not limited to, Magnetic Flux Leakage, Magnetic Particle Inspection, Alternating Current Field Measurement and Eddy Current Testing. Due to its wide usage in the industry, Eddy Current based NDT techniques are explained in a separate section in this chapter.

MPI procedure starts with the magnetization the system, either by introducing current (AC or DC, depending on the application) to it or applying a magnetic field from another source without introducing current. As a result of the magnetization, magnetic flux is created. When there is structural discontinuity in the system, there will be leakage of this flux in the proximity of the discontinuity. Following this process, magnetic particles are sprayed to the system. These particles will be accumulated next to the discontinuity, also called leakage field or stray flux. The accumulation of these particles then enables a visual indication about the existence and the location of the flaw. Using MPI technique, surface or near-surface breaks can be swiftly identified. Due to the good visual indication, training of the operating personnel is not hard either. However, MPI technique is only for ferromagnetic materials and flaws that are deep in the structure can't be identified **[21]**.

MFL inspection is quite similar to MPI procedure. After a magnetic field is induced to the test specimen using magnets, specimen is interrogated for structural discontinuities by checking for possible leakage flux. In contrast with MPI, leakage of the flux is detected by a detector coil or a Hall probe. Unlike MPI, MFL inspection is more sensitive to subsurface defects, though its sensitivity peaks near the surface. Due to its magnetic nature, though, it is only applicable to ferromagnetic materials, thus it is widely used for metal pipes **[22, 23]**.

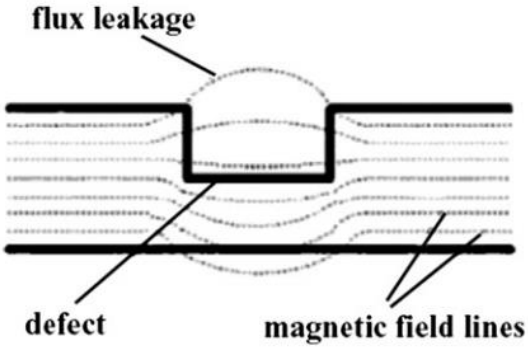

Figure 2-6 Schematic diagram of the flux leakage utilised in electromagnetic testing techniques. Image taken from [24].

ACFM technique introduces an alternating current to the test material using a probe. The uniform alternating current flows close to the surface of the test material and if there is no defect, the current will be undisturbed. If there is a defect, current flows around the defect. The associated magnetic field with the current is also disturbed in the presence of a defect, and this disturbance is captured with magnetic sensors. The magnitude of the captured magnetic field can then be used to size the defect as well **[25]**.

Unlike MPI and MFL, ACFM doesn't require the removal of surface coatings or paints in the test material and is a non-contact technique. Therefore, it is widely used for subsea inspection of offshore platforms. With proper modification of the ACFM system, it can also be used for inspection in environments with elevated temperatures. It can be used to inspect conductive materials, though in multiple-defect or small-defect cases, ACFM technique has its shortcomings [**5, 26**].

There are several other NDT methods which are not explained in this section, such as liquid penetrant testing, leak testing, laser based NDT methods, NDT techniques utilizing image processing/computer vision, noise monitoring and several other manual/visual inspection techniques. Some of these unexplained techniques are explained in the literature review parts of the upcoming sections if needed.

Using mechanical waves, or sound, to inspect structures is also a widely used technique too, ranging from conventional ultrasonic inspection to low frequency guided wave inspection. As the focus of this thesis is ultrasonic guided waves, conventional ultrasonic testing and ultrasonic guided waves are explained in more detail in the following sections.

2.3. :Conventional Ultrasonic Testing

Utilization of sound for the assessment of structures is a common technique in NDT industry. Ultrasonic testing systems are formed of transducers (either contact or non-contact) and a signal generation unit which drives the transducer. Transducers, when excited with a high voltage electrical signal, convert the electrical energy to mechanical waves (the mechanism of this conversion depends on the type of transducer) which propagates through the media. Generally, high frequency excitation ranging from couple of kHz to MHz range is used to induce mechanical waves to the test specimen. Once the

propagating wave encounters a structural discontinuity, which is basically a change of acoustic impedance, wave is either fully or partially reflected. This reflected wave is captured by the transducer and converted to an electrical signal, which can then be analyzed for finding where the defect is. In addition to detecting flaws, high frequency ultrasound can also be used for characterization and measurement of the dimensions of the material **[27].**

Ultrasonic testing has several advantages and disadvantages compared to other NDT techniques. As the excitation wavelength is considerably lower than the dimensions of the media, high frequency ultrasonic testing has good material penetration properties and also can detect small discontinuities, both surface and sub-surface flaws. Since the waves travel with constant speed, localization of the defects is considered as highly accurate. However, in many cases, contact with the test material is required. Moreover, certain cases require couplant for proper excitation. Although it is not a hazardous technique, thorough training of the operators is required. Lastly, due to its high frequency nature, waves are limited in their propagation distance (due to high attenuation); therefore manual scanning of the entire material is required for a complete evaluation, which makes it impracticable for interrogation of elongated structures **[28]**.

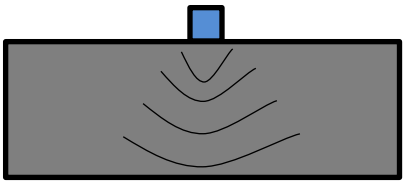

Figure 2-7 Representative diagram for an ultrasonic testing system. Blue object represents the transducer; the wave propagating through the material is shown with curves.

Waves propagating through media in high frequency ultrasonic testing are called **bulk waves**. Due to the difference between the dimensions of the media and the wavelength of the wave, such media are called *infinite* or *unbounded.* As the name implies, there are no boundary conditions to include in its mathematical equations. The information on bulk wave propagation in unbounded media is well documented **[29]**, and it is also explained briefly as follows.

There are two types of bulk waves which propagate independent of each other; shear and longitudinal. Assuming constant density, homogenous, linear elastic and isotropic materials, the derivation of the mathematical equations starts with *Euler's equation* of *motion* (external forces are excluded as well). Starting with the derivation of *Euler's equation* of *motion* from *Newton's second law*, if one relates the stress tensor to the strain tensor, *Navier's equation* of *motion* can be obtained. *Helmholtz decomposition* on the *Navier's equation* yields the set of equations known as *Helmholtz differential equations*, which are given as

$$\nabla^2\varphi - \frac{1}{{C_l}^2}\frac{\partial^2\varphi}{\partial t^2} = 0 \qquad\qquad \nabla^2\mathbf{H} - \frac{1}{{C_s}^2}\frac{\partial^2\mathbf{H}}{\partial t^2} = 0 \qquad\qquad \textbf{2.1}$$

where **H** and φ are the curl of a vector potential and sum of a scalar compressional gradient, respectively. C_l and C_s, longitudinal and shear wave velocities are given as

$$C_s = \sqrt{\frac{\mu}{\rho}} \qquad C_l = \sqrt{\frac{\lambda+2\mu}{\rho}} \qquad \textbf{2.2}$$

where ρ is the material density, and μ (dynamic viscosity) and λ (first parameter) are *Lamé constants* **[30]**. *Helmholtz differential equations* can also be expressed as in the following form

$$\varphi = A_l e^{i.(k_l.r-\omega t)} \qquad \mathbf{H} = A_s e^{i.(k_s.r-\omega t)} \qquad \textbf{2.3}$$

where As and A_l are the magnitudes of the shear and the longitudinal wave propagating in direction *r,* and k_s and k_l are the wavenumbers of the waves **[31]**. Wavenumber vectors, which are also given using the angular frequency ω and wave velocities, $C_{s,l}$, are as follows

$$k_{s,l} = \frac{\omega}{C_{s,l}} \qquad \textbf{2.4}$$

There is another wave mode called Rayleigh waves, which propagates along the surface of a semi-infinite media. First investigated by John Strutt in 1885, such waves are often encountered in natural phenomena like ocean waves and earthquakes **[32]**. Rayleigh wave motions are a combination of longitudinal and shear displacements and acts in an elliptical manner where the displacement of the wave is the highest on the surface of the media. The displacement decreases exponentially with the depth of the material, making Rayleigh waves most suitable for surface interrogation in NDT context. Rayleigh wave velocity is not dependent on frequency, but dependent on material properties such as Poisson's ratio, Young's modulus and density. Rayleigh wave velocity is given as

$$C_r = \frac{0.87+1.112\mu}{1+\mu}\sqrt{\frac{E}{\rho}.\frac{1}{2\mu+2}} \qquad \textbf{2.5}$$

where ρ is the material density, E is the Young's modulus and μ is the Poisson's ratio. Rayleigh waves are often used in geophysics, communications and various NDT applications **[33].**

2.4. :Ultrasonic Guided Waves–based Testing

As shown in Rayleigh wave case, under certain circumstances, unlike bulk waves, there might be boundaries that constrain the wave propagation. Rayleigh wave exists when there is a single boundary, which effectively guides the wave, thus the name *waveguide*. In several cases, there might be multiple boundaries guiding the propagating wave. Such waves are called *guided waves,* and they exist in many different modes depending on the frequency spectrum of the propagating wave, material geometry and properties. In contrast with bulk waves, guided waves potentially exist in infinite number of modes which propagate in different mode shapes, which means further complexity is introduced. Propagation of numerous modes in different shapes also leads to frequency-dependent velocity during propagation, also called *dispersion*, which will be discussed in the following parts of the thesis as a separate section.

From a physics standpoint, guided waves must satisfy equations of motion described in bulk wave propagation section, and also the boundary conditions which vary dramatically with respect to the media. These additional constraints mean complexity of obtaining analytical solutions, or lack thereof in

some cases. Guided wave propagation, as its boundary conditions depend on the geometry of the media, can be analyzed into two subsections; guided waves in plates and cylindrical structures. Guided waves in cylindrical structures are analyzed more in depth since this thesis focuses on guided waves in multi-wire helical wave guides, which is more related to cylindrical wave modes rather than plate-wave modes.

2.4.1. :Guided Waves in Plates

Guided waves in plates are investigated initially by Lamb **[34]**. By manipulating the work of Rayleigh for a finite media, Lamb showed that there are an infinite number of possible wave modes propagating in a plate structure, which are classified based on their particle displacement; symmetric wave modes which have symmetric particle displacement through mid-plane of the plate, or asymmetric wave modes which have opposite and asymmetric particle displacement through mid-plane of the plate. Propagation characteristics are also shown to be dependent on the wave mode and the thickness of the plate structure.

It is also known that as the frequency is increased, waves propagate in a way that additional wave modes appear. These so called *higher-order modes* are still either symmetric or asymmetric like the fundamental Lamb wave modes, though displacement characteristics of higher order modes is more complex. The conventional way of representing plate-wave modes is to A_x and S_x, where *A* and *S* stand for symmetric and asymmetric modes, respectively. Subscript *x* indicates the wave number, 0 indicating the fundamental modes and increasing numbers indicating the higher order modes having more complex displacement characteristics.

2.4.2. :Guided Waves in Cylindrical Structures

Earlier investigations of guided waves in cylindrical structures are performed by Chree and Pochhammer **[35, 36]**, which are then succeeded by the work of Gazis **[37, 38]** who managed to present an analytical solution to guided wave propagation in such structures. Similar to plate waves, it is shown for cylindrical structures that there might be an infinite number of wave modes propagation through the structure, which is again classified by their particle displacement. Although the detailed derivation of the analytical solutions can be found in [**38**], a brief discussion is provided in this section to give the reader an insight about the subject matter.

As discussed in bulk wave section, the analytical derivation starts with applying Helmholtz decomposition on Navier's equation of motion, but in this case in cylindrical coordinates. Firstly, if Navier's equation of motion is solved in the form of cylindrical coordinates, one gets

$$\varphi, \mathbf{H} = \Gamma_{\varphi,\mathbf{H}(\mathrm{r})}\Gamma_{\varphi,\mathbf{H}(\theta)}\Gamma_{\varphi,\mathbf{H}(\mathrm{z})}e^{i.(k.r-\omega t)} \qquad \textbf{2.6}$$

where $\mathbb{\Gamma}_{\varphi,\mathbf{H}()}$ terms represent the coordinate variation, r represents the position vector and r, θ , and z represent the spatial coordinates. Helmholtz decomposition then can be represented as

$$\varphi = f(r)cos(n\theta)e^{i.(\xi.r-\omega t)}$$

$$\mathbf{H_r} = g_r(r)sin(n\theta)e^{i.(\xi.r-\omega t)}$$
$$\mathbf{H_\theta} = g_\theta(r)cos(n\theta)e^{i.(\xi.r-\omega t)}$$
$$\mathbf{H_z} = g_3(r)sin(n\theta)e^{i.(\xi.r-\omega t)} \quad \textbf{2.7}$$

where ξ is the wavenumber in z direction **[38]**. After performing certain algebraic procedures, displacement fields are presented as

$$u_r = cos(n\theta)e^{i.(\xi.r-\omega t)}[f' + g_3\frac{n}{r} + \xi g_1]$$
$$u_\theta = sin(n\theta)e^{i.(\xi.r-\omega t)}[-g_3 - f\frac{n}{r} + \xi g_1]$$
$$u_z = cos(n\theta)e^{i.(\xi.r-\omega t)}\left[-g'_1 + \frac{g_1}{r}(n+1) - \xi f\right] \quad \textbf{2.8}$$

where f(r), g_1(r) and g_3(r) are potential functions, which are described in detail in [**37**]. Lastly, if stress is rewritten as a function of displacement, one gets

$$\sigma_{rr} = [\,-\lambda(\alpha^2+\xi^2) + 2\mu\left(f'' + \frac{n}{r}\left(g'_3 - \frac{g_3}{r}\right) + \xi g'_1\right]cos(n\theta)e^{i.(\xi.r-\omega t)}$$
$$\sigma_{r\theta} = \mu\left[-2\frac{n}{r}\left(f' - \frac{f}{r}\right) - \left(2g''_3 - \beta^2 g_3\right) - \xi\left(\frac{n+1}{r}g_1 - g'_1\right)\right]sin(n\theta)e^{i.(\xi.r-\omega t)}$$
$$\sigma_{rz} = \left[-2\xi f' - \frac{n}{r}\left(g'_1 + \frac{n+1}{r}g_1\right) + (\beta^2 - \xi^2)g_1 - \frac{n\xi}{r}g_3\right]cos(n\theta)e^{i.(\xi.r-\omega t)}$$
$$\alpha^2 = \frac{\omega^2}{c^2{}_l} \qquad \beta^2 = \frac{\omega^2}{c^2{}_s} - \xi^2 \quad \textbf{2.9}$$

where c_l and c_s are longitudinal and shear velocities, and ω is the angular frequency.

As can be derived from the equations above, there are two types of wave modes in cylindrical structures; axisymmetric wave modes which have uniform displacement around the circumference of the structure and flexural wave modes which have harmonic displacement around the circumference. Axisymmetric wave modes are then divided into two modes; longitudinal wave mode that has displacement in either R or Z planes, and torsional wave mode that has displacement in θ plane. Flexural wave modes have displacement in all planes. The convention used to represent guided wave modes in cylindrical structures is slightly different than plate-wave modes. Assuming a form of *A(x,y)* to represent cylindrical wave modes, *A* refers to the name of the wave mode (Longitudinal, torsional or flexural) and replaced by L,T or F. The term *x* refers to the harmonic variations in displacement around the circumference and *y* refers to the order of the mode since higher order modes appear in the high frequency regions. As one can observe, *x* will be zero for longitudinal and torsional wave modes, though it will vary for the flexural wave mode **[39]**.

2.4.3. :Dispersion Curves

As briefly mentioned previously, guided waves tend to travel with varying speeds depending on the frequency spectrum of the wave. In order to understand dispersion phenomenon, two concepts are required; phase and group velocity.

The propagation of an ultrasonic guided wave happens by the change in the phase, which is defined as the phase velocity of the signal. A more formal definition is the velocity of a single frequency in a wave, which is calculated using wavenumber *k*

$$C_{ph} = \frac{\omega}{k} \quad \textbf{2.10}$$

Group velocity, which is the velocity of the entire signal also called the *envelope*, can be derived using the phase velocity as **[27],**

$$C_{gr} = C_{ph} + k\frac{dC_{ph}}{d_k} \quad \textbf{2.11}$$

Although phase velocity and group velocity could be the same, there are cases where they are not. This means the certain frequency components in the signal (phase velocity) will be travelling with a different speed than the entire wave packet (group velocity). This results into the broadening of the excited signal (in UGW applications, generally a short duration pulse). In order to have a complete understanding of the phase and group velocity values with respect to frequency, as well as the cut-off frequency (the frequency they appear) of the higher order wave modes, *dispersion curves* are used. By looking at the group and phase velocity dispersion curves, wave modes and their dispersiveness can be seen. It must be noted that dispersion curves depend on material geometry and properties; hence they must be calculated for every application.

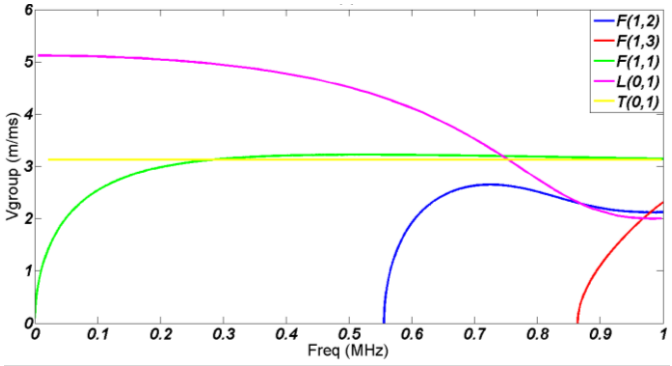

Figure 2-8 An example dispersion curve for an aluminium wire of 3.4 mm diameter. Shown curves are fundamental torsional (yellow), fundamental longitudinal (magenta), fundamental flexural (green) and two higher order wave modes.

Modes that have constant speed over a frequency range are called non-dispersive. These modes inherently tend to have close phase and group velocities. Dispersion curves are crucial for practical use of ultrasonic guided waves in NDT because one can look at the dispersion curves for a structure and then decide which frequency range to use or which wave mode the excitation needs to be optimized for. Dispersion curves are analytically studied by Gazis and Viktorov **[38, 40]**. One of the widely used software called Disperse, which is used throughout this thesis, uses Global Matrix Method to calculate dispersion curves. Detailed information about Global Matrix Method can be found in **[41]**.

Although it depends on the geometry and the material properties of the structure, in the name of practicality, one might say by looking at the figures above that the fundamental torsional wave mode tends to be non-dispersive. Moreover, higher order flexural and longitudinal wave modes appear at

higher frequencies and these wave modes tend to be less-dispersive in high frequencies. However, that doesn't mean that high frequency region is more desirable as it is non-dispersive because attenuation is generally higher in such cases.

2.5. : Critical Summary

Having presented the fundamentals about NDT and most important concepts about UGW, next chapter builds on the presented knowledge and introduces an important part of this research, wherein the wave propagation is experimentally analyzed for a specific type of OVTL cable (ACSR). A comparison between theory and experimental results are provided along with a detailed defect detection analysis, as well as an empirical study to find an optimum excitation configuration for extended inspection range.

CHAPTER 3: Ultrasonic Guided Waves in OVTL Cables

3.1. :Overview

This chapter forms the backbone of the thesis; it introduces the concept of guided waves for NDT purposes and the actual motivation of research, which is the inspection of power line cables. Inspection of Overhead Transmission Line (OVTL) cables is performed using various Non-Destructive Testing (NDT) techniques, such as visual, temperature and eddy current-based inspection; yet each have their respective shortcomings and safety concerns. The use of Ultrasonic Guided Waves (UGW) as an NDT technique is well established for simple geometries such as plates, pipes and rods; but for multi-wire cables (i.e. OVTL cables) it is relatively in early stages. In this chapter, utilisation of UGW as a defect detection technique is investigated. Aluminium Conductor Steel Reinforced (ACSR) cable specimens are evaluated using a collar formed of shear mode Lead Zirconium Titanate (PZT) transducers. Identification and analysis of wave propagation for a broad range of frequencies is performed via Laser Scanning Vibrometry (LSV), and the effect of defect size on wave propagation is studied accordingly. Defects that correspond to 4.5% reduction in cable Cross Sectional Area (CSA) are successfully detected.

3.2. :Introduction

Multi-wire cables are extensively used in broad spectrum of engineering applications to meet various demands; such as load carrying in bridges, cranes and elevators; post-tensioning in concrete structures; and electricity transfer in power grids. OVTL cables of different structural properties used in power grids span long distances and form the backbone of the energy distribution grid. Throughout their service life time, OVTL cables are influenced by various effects such as operational factors (applied tensile stress and voltage stress), environmental factors (wind-induced vibrations, icing, melting and lightning strikes) and man-caused vandalism. Those factors, especially if the specimen has structural imperfections due to faulty manufacturing, result in structural failures such as broken insulators, loose earth conductors, mechanical failures (twisted/ruptured/broken wires) and corrosion **[42, 43]**. Structural failures start emerging in aluminum layers first, and if proper care is not taken, steel core can have failures too **[44]**, though in some cases steel core is reported to be intact even though aluminium layers had structural failures **[42]**. Consequences of a structural failure in OVTL cables is reported in **[44]**, where the failure of ACSR cables left 67 million people under power blackout in Brazil. Therefore, a reliable and fast inspection system, preferably an automated one with minimum human involvement is desirable.

Certain NDT techniques have emerged and been widely used to provide pre-emptive measures against structural failures. Airborne and on-ground visual inspection performed by trained personnel is one of the first methods devised for structural maintenance of OVTL cables. It requires extensive care from personnel **[45]** and it is subject to regulations **[46]**. Manual visual inspection, however, is time-consuming, prone to human errors and has associated health hazards; primarily for airborne inspections where helicopter crashes resulted in loss of lives **[47]**. In order to avoid human error and reduce health hazards, recent inspection methods have used different techniques to automate inspection systems. Automated visual inspection systems have been developed which apply image processing algorithms on

videos/images acquired by either installed camera systems or airborne image acquisition systems. The efficiency of those methods relies heavily on the quality of the acquired images, thus the quality of the camera and the stability of the aerial vehicle **[48].** Temperature inspection methods have been proposed in **[49]** and **[50]**, where infrared cameras are used to collect images of the power line components to detect corona effects triggered by structural discontinuities. Eddy current-based systems for the inspection of OVTL cables are reported in **[51]** and **[52]**, where eddy currents are utilised for the detection of broken strands and corrosion on an OVTL cable. Kasinathan et.al has described in **[53]** the utilisation of fibre optic cables for temperature monitoring of OVTL cables to extract structural integrity information. Radio and audible noise monitoring to acquire structural health information has also been proposed for OVTL cables [**54**]. In order to increase inspection range and quality, some studies have also utilised advances in robotics for inspection of OVTL cables. Use of robotics, however, has its respective disadvantages, such as complexity in design, maintenance of robots, electromagnetic interference introduced by high current to communication systems of remote controlled robots, optimisation of weight and line tracking abilities for Unmanned Aerial Vehicles (UAV) **[48]**. In order to tackle design complexity, human errors and health hazards associated with above mentioned methods, UGW based NDT methods have been investigated.

UGW based NDT techniques have been utilized for the interrogation of various multi-wire cable structures, and studies related to guided wave characterization and defect detection in multi-wire cables have emerged. Xu et.al utilized magnetostrictive transducers to generate UGW for defect detection in seven-wire steel pre-stressing strands **[55]**, and also investigated guided wave-based defect detection of 31 and 37-wire stay cables **[56]**. Liu et.al studied the optimization of magnetostrictive transducer configuration to enhance guided wave inspection quality **[57]**. Studies have also emerged focusing on the possible effects of various factors that affect the wave propagation in multi-wire cables. Rizzo et.al studied ultrasonic wave propagation in seven-wire steel strands and analysed the changes in wave propagation with progressive loads applied on the cable **[58]**. Liu et.al also analysed the effects of temperature on wave propagation in multi-wire steel strands and related the wave propagation velocity variations to temperature changes **[59]**. The emphasis was also given to ACSR cables in several UGW based NDT studies. Haag et.al investigated guided wave propagation in ACSR cables with the aim of understanding energy transfer between wires, and formulated a computationally efficient energy-based model to predict wave propagation in a simplified two-rod system with friction contact **[60]**. Branham et.al reported the feasibility of defect detection in ACSR cables with two different transducer coupling schemes and an understanding of attenuation and dispersion in ACSR cables **[61]**. Gaul et.al reported an overall feasibility analysis of the use of guided waves for damage detection in ACSR cables with an emphasis on reflection of wave packets at structural discontinuities with varying geometry and size **[62]**. In one of the latest studies, Baltazar et.al investigated the changes in guided wave propagation in ACSR cables in the presence of a defect, and reported that the energy of the flexural modes changes when a defect is introduced and this change can be monitored for defect detection **[63]**. However, the above mentioned studies have neither reported an investigation of UGW-based inspection with an aluminium-layer emphasis nor the inspection efficiency for long OVTL cables under noisy (i.e. measurement noise, random noise, etc…) conditions.

This chapter of the thesis is structured as follows. In Section 3, methodology used in this work is presented. Section 4 provides the necessary information about the cable and the hardware used in this work. Section 5 and 6 present the experimental setups and necessary theoretical information for wave propagation characterization and defect detection respectively. Results of Section 5 and 6 are presented in Section 7.

3.3. :Methodology

Reliable and efficient design of an NDT system requires thorough understanding of wave propagation in the medium of concern. Evaluation of transducer coupling and respective analysis of wave propagation should be performed to achieve optimal results. Figure 1 shows the adopted methodology for this study.

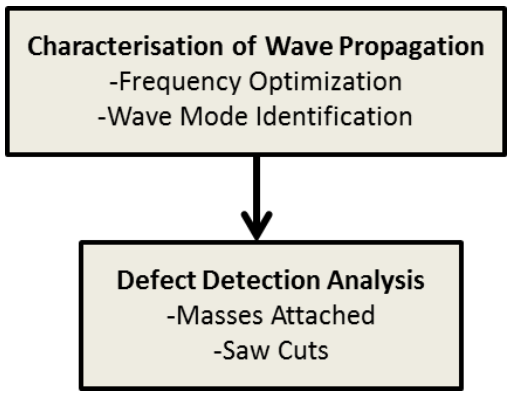

Figure 3-1 Flow diagram of adopted methodology.

Characterisation of wave propagation is performed in two stages. Based on the real life structural failures that have been reported **[42, 44]**, the priority of inspection of ACSR cables is given to aluminium layers. Firstly, excitation frequency optimisation is performed with the aim of concentration of the energy on the aluminium layers of the ACSR cable through LSV experiments. Optimisation of the energy by correct frequency selection would ideally provide an extended inspection range. Afterwards, wave propagation on the surface is identified via LSV experiments. Acquired signals in this part are then analysed using Short-Time Fourier Transform (STFT) for comparison with the theoretical group velocity dispersion curves of single aluminium wire (forming inner and outer layers of ACSR cable), which are calculated via commercially available Disperse **[41]** software. Identification of optimised frequency band and ideal wave mode for inspection are then used for defect detection analysis.

Defect detection analysis is performed in two different ways; attaching masses around the cable and by machining a saw cut into the cable with gradually increasing cut depths. A wide signal database is created using a broad range of excitation frequencies for accurate identification of an ideal defect detection frequency. Final evaluation of the identified excitation frequency is presented; detectable smallest cut depth is reported. Feasibility of real-life application of the system is discussed and the need for signal processing techniques is outlined.

3.4. :Cable Information and Instrumentation

ACSR cables are one of the most widely used power transmission line cables and they are made of aluminium and steel wires. The diameter of the individual wires and number of wires forming the cable vary between different ACSR cables. The cable used in this study, which has the codename *Bear 325*, has an overall diameter of 23.45 mm and consists of an inner core composed of seven steel wires, which are covered in anti-corrosive grease, and two outer layers of 12 and 18 aluminium wires respectively. The wire strands are twisted into a helical shape with each layer being twisted in the opposite direction. The evaluated ACSR cable specimens in all the experiments described in this thesis have the same structural properties (diameter, material, pitch, wire configuration, etc…) but varying lengths. Table 1 provides information with regards to the structure of the cable under investigation. Figure 2(b) illustrates the CSA of the cable.

Table 3-1 Cable Information.

Material	**Number of Layers**	**Wire Diameter [mm]**	**Number of Wires**	**Other Features**
Steel	1	3.4	7	Core Diameter: 10.05 mm
Aluminium	2	3.4	Inner Layer:12 Outer Layer:18	Surface Pitch: 300 mm

The transducer collar designed and manufactured for this study is illustrated in Fig. 2(a). The collar consists of 6 shear-mode PZT broadband transducers with sufficiently flat response in the frequency range of concern (up to 500 kHz). The transducer collar is connected to a Teletest Focus **[64]**, a commercially available Long Range Ultrasonic Testing (LRUT) system. Experimental results are acquired using Teletest Focus unit (except LSV experiments) with 1 MHz sampling frequency (both TX and RX) and then transferred to a computer for analysis and post-processing in MATLAB. Power gain levels varied with experiments; 20 dB for LSV experiments and 37 dB for defect detection experiments. Signals exciting the transducers, depending on the goal of the experiment, ranged from broadband pulses to Hann-windowed 10-cycle single tone burst excitations with different centre frequencies.

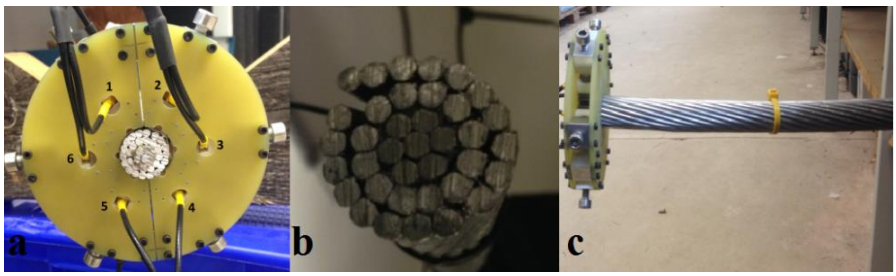

Figure 3-2 Photographs of (a) 6- shear mode PZT transducer collar, (b) cable cross section and (c) transducer collar mounted on the cable.

3.5. :Characterisation of Wave Propagation

3.5.1. :Frequency Optimisation

Frequency optimisation for aluminium layer-inspection emphasis is performed by using a *PSV-400 PolyTec* LSV **[65]** on a 2-metre long ACSR cable specimen. Cross section of the cable end where transducer collar is attached is scanned via LSV. Transducers are driven with broadband (up to 500 kHz) pulse excitation signal. The number of scan points are optimised in the scan area (cross-section of the cable) to have appropriate resolution of energy penetration in the cable. Signal acquisition for each scan point is averaged 70 times to have accurate signal-to-noise ratio (SNR). A representative diagram for LSV experiments is given in Fig. 3. Light green circle covering the CSA of the cable indicates the area scanned.

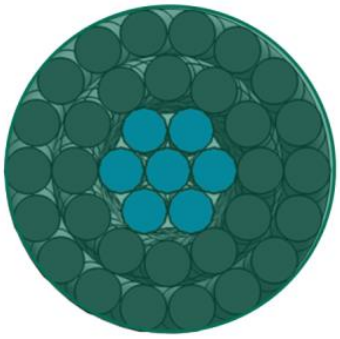

Figure 3-3 Schematic diagram of the cross section of the cable showing the LSV Scan area.

3.5.2. :Wave Mode Identification

3.5.2.1.1. :Theoretical Approach

Guided wave theory is well established, and its characteristics can be represented with analytical solutions for structures such as pipes, plates and rods **[34]**. Helical multi-wire strand structures, due to complex geometry and non-linear contact between individual wires, don't have analytical solutions which can describe wave propagation in depth. Even though there are studies aimed to provide a better understanding on wave propagation for helical multi-wire waveguides **[66, 67**], this study considers the wave propagation in a simplified structure (solid cylindrical rod) and analyses wave propagation for single-wires forming the ACSR cable.

On the single-wire level, group velocity dispersion curves for single wires of ACSR cable (3.4 mm diameter steel and aluminium) are acquired using Disperse **[41]** software. Results are shown in Fig. 4.

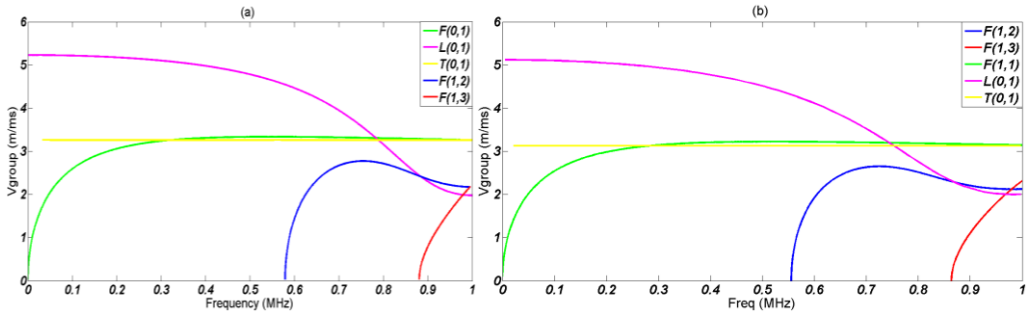

Figure 3-4 Single-wire group velocities for (a) 3.4 mm diameter steel and (b) 3.4 mm diameter aluminum.

Figure 4 shows five wave modes both for steel and aluminium up to 1 MHz; three fundamental wave modes and higher order flexural modes. Above 500 kHz, there are two higher order modes that are highly dispersive and slow. The fundamental flexural mode is also slow and it exhibits dispersive characteristics in low frequency band (<200 kHz). Fundamental torsional and longitudinal modes appear to be suitable for defect detection both for steel and aluminium, though longitudinal is much faster than torsional in low frequencies yet slightly dispersive. Theoretically, due to its speed and relatively low dispersive behaviour, longitudinal mode seems ideal for defect detection. Due to the fact that emphasis is given to aluminium layer inspection, experimental dispersion curves should be in agreement with curves shown in Fig. 4(b). Extent of this agreement is investigated in the following sections.

3.5.2.1.2. :Vibrometry Analysis

Experimental identification of wave modes is conducted via LSV experiments using a 2 meter long ACSR specimen. Two different experimental configurations are adopted. Representative diagrams for experimental setups are given in Fig. 5.

The light green areas indicate the scanned areas. In the first configuration, a grid scan on the surface of the cable is performed, shown in Fig. 5(a), and transducers are excited with Hann-windowed 10-cycle single tone burst excitation signals with randomly picked frequencies (20-125-250 kHz) and also a broadband pulse (up to 500 kHz). This configuration aims to identify the present wave modes and also the dynamics of wave propagation on the surface. In the second configuration, shown in Fig. 5(b), an individual surface aluminium wire is chosen and scanned. In this case, a broadband pulse excitation (up to 500 kHz) is used to drive the transducers. This second configuration aims to quantitatively identify dispersion curves in wave number – frequency domain.

In both configurations, scan points are optimised to have a sufficient resolution of wave propagation. The signal acquired for each individual scan point is averaged 70 times to have better SNR. Scan areas in both configurations had 1.5 cm height and distances between scan points are well-tuned to have equal spacing between them.

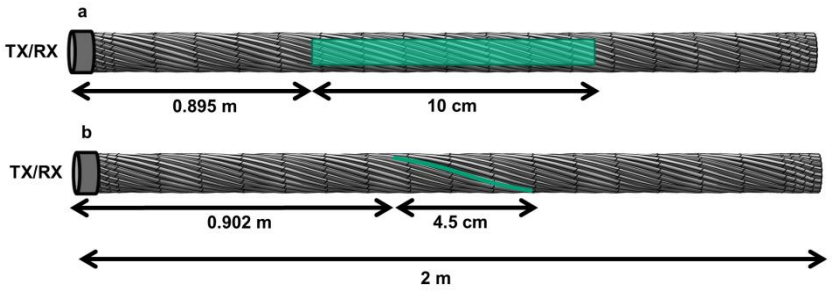

Figure 3-5 Diagram illustrating the geometry of the LSV (a) grid scan covering multiple wires and (b) a line scan over an individual wire.

3.6. :Defect Detection Analysis

Defect detection analysis is performed on a 26.5 meter long ACSR cable in pulse-echo configuration, similar to LSV experiments. Figure 6 illustrates the experimental setup used in this section.

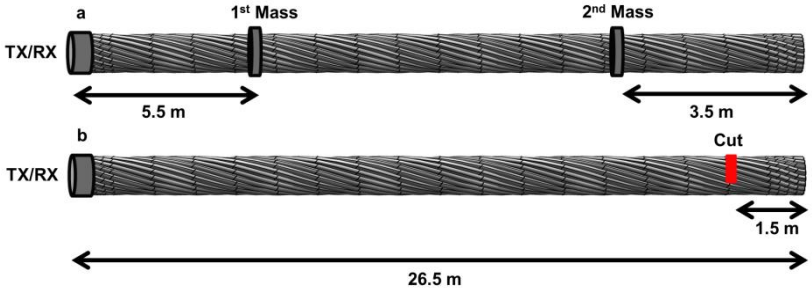

Figure 3-6 Schematic of pulse-echo experiment for 26.5 m cable showing (a) masses attached to the cable and (b) saw cuts introduced into the cable.

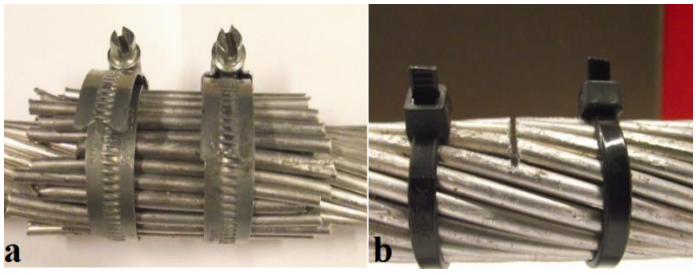

Figure 3-7 Photograph of (a) Masses attached on the cable and (b) 6.5 mm-deep, 1 mm-wide saw cut.

Excitation signals driving the transducers in this section are chosen as Hann-windowed 10-cycle single tone burst excitation. A frequency sweep is performed between 20 and 350 kHz to find the best frequency for the wave guide. In order to simulate defects, two different schemes are adopted; attaching masses and introducing cuts to the cable.

UGW-based NDT systems, to detect defects, rely on partial or complete reflection of the guided wave when it hits a structural discontinuity. Structural discontinuities can exist in different forms and orientations. In cylindrical structures, structural discontinuities lead to changes in CSA, either positive or negative. In the first scheme, defects which introduce an increase in CSA are investigated. Individual aluminium wires are taken off from another cable specimen and attached around the circumference of the cable and then tightened with a clip, as illustrated in Fig.

7(a). Attaching masses before introducing actual cuts to the cable is also a feasible method of preliminary experimentation, since attaching masses doesn't damage the structural integrity of the cable. In this part, first a set of additional aluminium wires are attached to 23 metres from the transducer collar. Afterwards, second set of additional aluminium wires are attached to 5.5 metres from the transducer collar. Representative diagram of this experimental setup is shown in Fig. 6(a).

In the second scheme, defects, which introduce a decrease in CSA, are investigated. Towards this end, transversal notch cuts are introduced to the cable with a saw, as shown in Fig. 7(b). Transversal cuts are machined into the cable 25 metres from the transducer collar and cut depth is gradually increased from 2.5 mm to 6.5 mm, which corresponds to approximately 4.5% to 30.7% reduction in CSA of the cable. Representative diagram of this experimental setup is shown in Fig. 6(b).

3.7. :Results

3.7.1. :Wave Propagation Characterization

3.7.1.1. :Frequency Optimization

Figure 8(a) shows velocity values in dB for all scan points for a single frequency and Fig. 8(b) shows velocity FFT for each direction in dBs for a scan point in an aluminium layer (shown as blue rectangle in Fig. 8(a)).

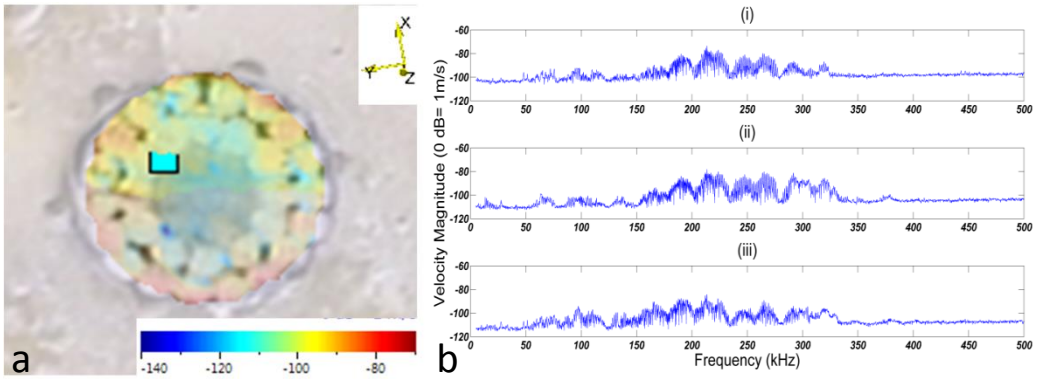

Figure 3-8 CSA FFT scan results of (a) velocity values in dB for ~223 kHz (representative frequency) and (b) velocity FFT of a single scan point for x, y and z directions (i to iii) (inner aluminum wire).

Visualisation of energy concentration for different frequencies is needed to accurately identify frequency regions where wave energy is pronounced on aluminium layers. Towards this end, it is assumed that surface aluminium layer will always have more energy than inner aluminium layer due to coupling of the transducers to the outer aluminium layer. Based on this assumption, a scan point has been chosen on the inner aluminium layer and the velocity values in each direction have been analysed. In Fig. 8(b), it can be seen that wave energy is high in-between 200 and 300 kHz range. This frequency band concentrates the energy band on the aluminium layers. This concentration is also verified in Fig. 8(a); a frequency is chosen randomly in 200-300 kHz range (~223 kHz) and it is apparent that the wave energy is well concentrated on each of the aluminium layers.

3.7.1.2. :Wave Mode Identification

Figure 9 shows three dimensional velocity values for 20, 125 and 250 kHz excitation at the times where each signals' velocity value is at its peak. Figure 10 illustrates velocity in each direction for 20, 125 and 250 kHz excitations for the scan point shown as light blue rectangle in Fig. 9, which is the point where 3D velocity peaks for 250 kHz excitation.

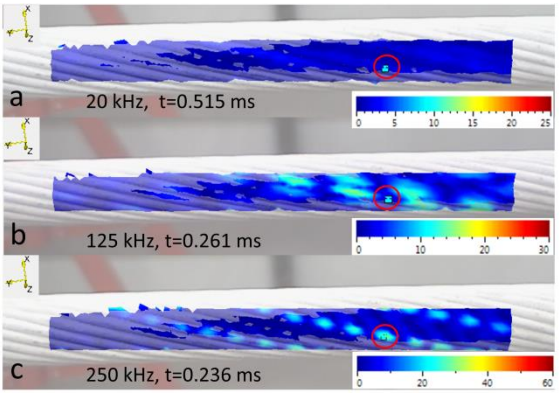

Figure 3-9 3D-velocity values are shown (in dB) for surface scan configuration shown for various frequencies at times where velocity values peak; (a) 20 kHz (t=0.515 ms in Fig. 10 (a-b-c)), (b) 125 kHz (t=0.261 ms in Fig. 10 (d-e-f)), (c) 250 kHz (t=0.236 ms in Fig. 10 (g-h-i)).

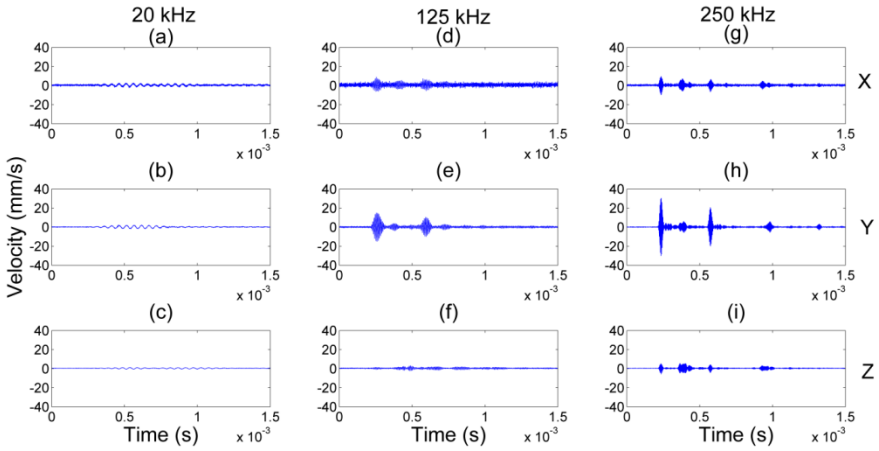

Figure 3-10 Graphs of the LSV measured velocities, for the point on the cable shown in Fig. 9, in the X-Y-Z axis directions for (a-b-c) 20 kHz, (d-e-f) 125 kHz, (g-h-i) 250 kHz.

Among all the frequencies shown in Fig. 9, 250 kHz excitation has the highest velocity on the surface. For a fixed scan point (light blue rectangle in Fig. 9), as shown in Fig. 10, velocity time traces of each direction for three signals also show a great increase as the frequency increases, making 250 kHz the best choice among the frequencies shown. This frequency is in good agreement with the frequency range obtained in the previous section (200-300 kHz) as well. Energy transfer between adjacent wires is also visible, though energy is generally concentrated on individual wires that have direct coupling with the transducers. The propagation of the wave through individual wires rather than the cable as a whole also raises the necessity of an accurate calculation of the travelled path distance. For a cable with a

length *L=N.t*, in order to find the actual travelled distance by the waves, helical length should be found as,

$$L_{Helical} = N.\sqrt{\pi^2.d^2 + t^2} \qquad \textbf{3.1}$$

where *N* is the number of turns, *t* is the pitch and *d* is the diameter of the helix. From here onwards, time-of-arrival calculations are calculated with helical length correction taken into account.

Following the analysis of the wave propagation on the surface, identification of the wave modes is performed using the experimental setup illustrated in Fig. 5(a) with a broadband (up to 500 kHz) excitation signal. Illustrated in Fig. 11 are STFT representations of velocity in three directions for the vibrometer scan point shown in Fig. 9. Theoretical group velocity dispersion curves for aluminium wire are used to find arrival curves, calculated as *propagation distance divided by group velocity of the wave modes* shown in Fig. 4(b). Arrival curves are then overlaid on STFT representations of analysed data.

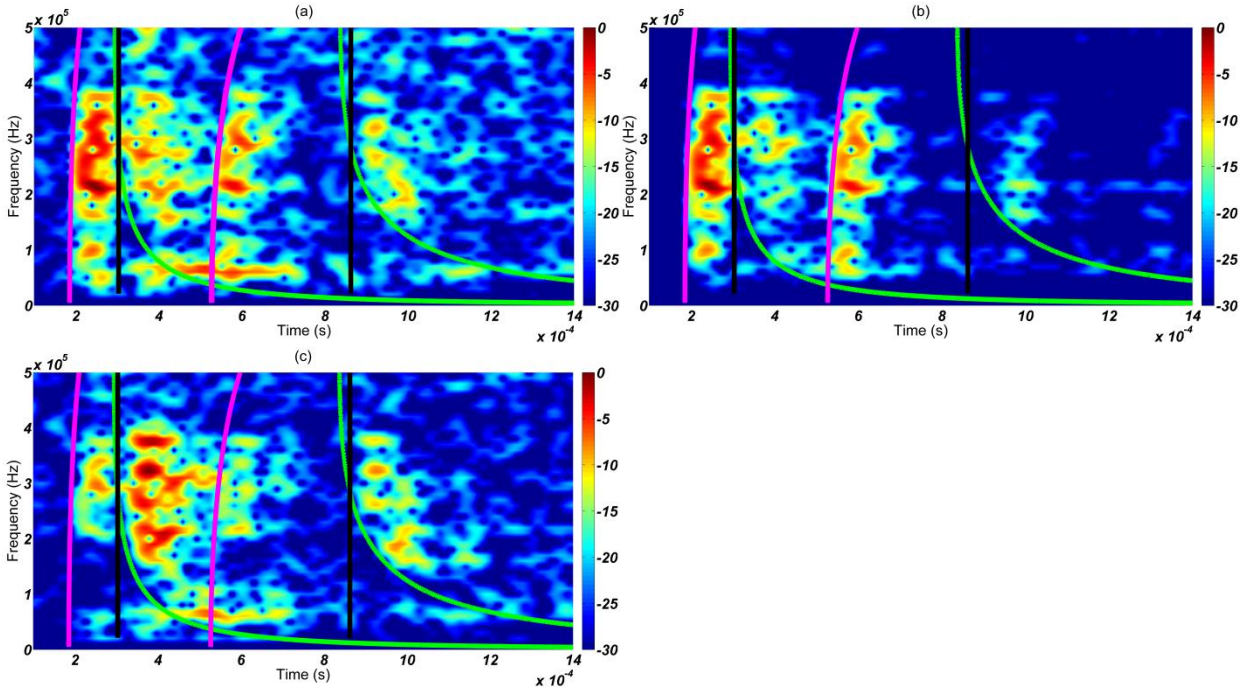

Figure 3-11 Graphs show Short-Time Fourier of velocity for broadband pulse excitation with arrival curves overlaid for; direct arrival and first echo of L(0,1) magenta line, T(0,1) black line, and F(1,1) green in the (a) X, (b) Y, and (c) Z axes directions.

Velocity values in each direction show that four distinguishable wave packets are received by the vibrometer. Once arrival curves, for three fundamental wave modes shown in Fig. 4(b) are overlaid, it is clear that first wave packet is in good agreement with the fundamental longitudinal wave mode for each direction. Second wave packet, could be torsional or flexural since both modes have similar time-of-arrival. Nevertheless, the second wave packet appears to be the flexural mode since lower frequency region (<100 kHz) of the second wave packet accurately follows the arrival curve of the flexural wave mode. The main reason of its appearance is reported as the inter-wire contact-induced energy transfer in **[63].** Third and fourth wave packets are also in good agreement with fundamental longitudinal and

flexural mode's arrival curves, except in Y-direction where flexural wave mode attenuates and another echo of the longitudinal wave mode is apparent.

The received wave packets have their energy spread over the spectrum, mainly between 50 and 400 kHz. The most powerful frequency component in the spectrum is also observed to be between 200 and 300 kHz, which verifies the good energy concentration obtained in Fig. 8. Since 200-300 kHz band experiences the lowest attenuation, it can be preliminarily said that this frequency band is ideal for long range inspection. Moreover, flexural wave mode attenuates much faster than longitudinal mode; therefore, in contrast with the findings of **[63]**, longitudinal mode should be used for long range inspection.

Even though the agreement between theoretical single aluminum wire dispersion curves and experimental dispersion curves is quite good (as shown in Fig. 11), a quantitative analysis is required to find the experimental dispersion curves. Since the wave propagates through individual aluminum wires, LSV experiment configuration shown in Fig. 5(b) is used with a 500 kHz broadband excitation signal to acquire wave propagation through a single wire. Uniform distribution of scan points in space provides displacement data in time- distance domain, which can be converted to wavenumber-frequency domain when a two dimensional Fast Fourier Transform (2D-FFT) is applied. Transformed matrix, provided that spatial spacing meets the Nyquist criteria for spatial frequency **[68]**, ideally provides accurate experimental measurement of the dispersion curves. Fig. 12 illustrates the experimentally acquired dispersion curves and theoretical dispersion curves overlaid for single aluminum wire.

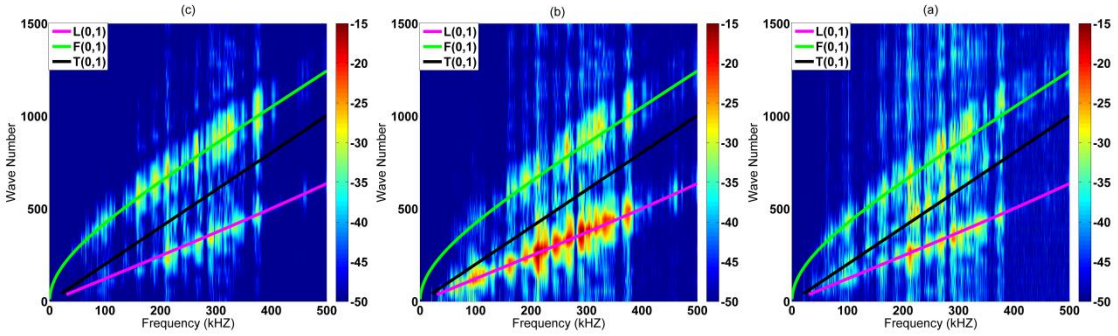

Figure 3-12 Experimentally measured dispersion curves in the wavenumber frequency domain for the (a) X, (b) Y and (c) Z directions. Overlaid are the theoretical dispersion curves, for aluminum rods of the same diameter as the wires, which were calculated using Disperse.

Figure 12 shows good agreement between theoretical dispersion curves of single aluminium wire shown in Fig. 4(b) and experimentally measured curves in each propagation direction. Therefore, once the correct path length is calculated via **(3.1)**, propagation of the wave through individual aluminium wires of the cable is found to be very similar to the single-wire case. Moreover, Fig. 12, similarly to Fig. 11, shows that the fundamental longitudinal mode is the most pronounced mode, whereas the fundamental torsional is non-existent except in X-direction propagation. The fundamental flexural mode is received, though it is more attenuative and dispersive; therefore, the fundamental longitudinal mode is the best wave mode for defect detection, as stated in the previous part. From here onwards, only the fundamental longitudinal mode is considered for defect detection.

3.7.1.3. :Defect Detection Analysis

3.7.1.3.1. :Masses Attached

RMS values of echoes reflected from masses are acquired for various frequencies. A window (with a constant size, enough to cover the entire wave packet for all excitation frequencies) is used to localise and calculate RMS values of the echoes. For different frequencies, due to change in group velocity of the longitudinal wave mode, the window is shifted accordingly to accurately localise and calculate RMS values. Figure 13 illustrates the results acquired in this section.

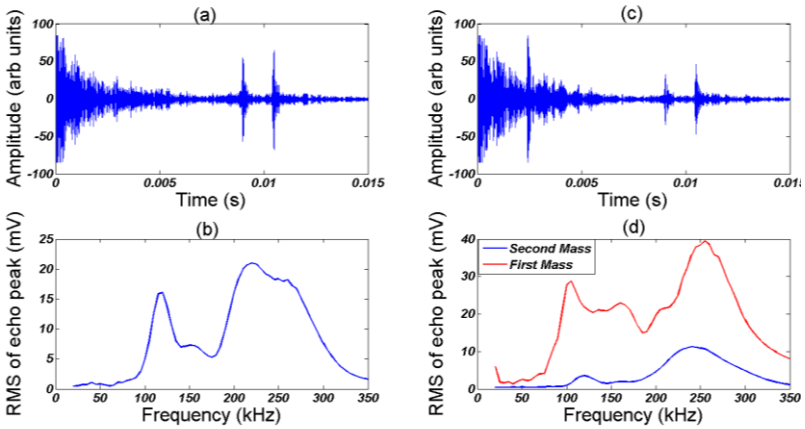

Figure 3-13 Graphs of a single mass attached on the cable for (a) 220 kHz excitation response and the (b) reflection echo RMS vs. frequency; two masses attached on the cable (c) 250 kHz excitation response and (d) reflection echoes RMS vs. frequency.

Figure 13(b) shows RMS values vs. frequency of one set of masses attached around the cable. In line with LSV analysis results, the RMS peak is observed to be between 200 and 300 kHz, and the peak is located at 220 kHz. Figure 13(a) shows time domain representation of 220 kHz signal with one set of masses attached; echoes from mass and cable end are visible. Figure 13(d) shows RMS values for each mass echo vs. frequency of two set of masses attached around the cable. The echo from the first mass (located 5.5 meters from the transducers) has higher RMS values due to its proximity to the transducers whereas echo coming from the second mass has lower RMS values. Both RMS values have their peaks in between 200 and 300 kHz, similar to only one mass attached result. RMS peaks of two mass echoes aren't at the same frequency; echo from the first mass peaks at 250 kHz whereas echo from the second mass peaks at 240 kHz. A compromise between a single excitation frequency and RMS values has to be made; in this case 250 kHz excitation is chosen and its time domain representation is shown in Fig. 13(c); echoes of both masses are visible. This compromise is also applicable to results of single set of masses attached too; RMS value peaks at 220 kHz but response of 250 kHz is really close to 220 kHz response. Therefore, 250 kHz is the best candidate for defect detection.

In addition to detectability of two defects at the same time, far end resolution of defect detection (minimum distance of a detectable defect from the end of the cable) in this section is found as 3.5

metres. Figure 13(a) and (c) show a time-gap between cable end and second mass' echo coming from the second mass, therefore, the far end resolution ideally could be lowered. Next section aims to analyse the detection of defects corresponding to decrease in CSA and establish a relationship between defect size and structural response.

3.7.1.3.2. :Saw Cut

RMS values of defect echoes are acquired for different defect sizes and various excitation frequencies using a constant-sized sliding window similar to previous section. Fig. 14 illustrates the results acquired in this section.

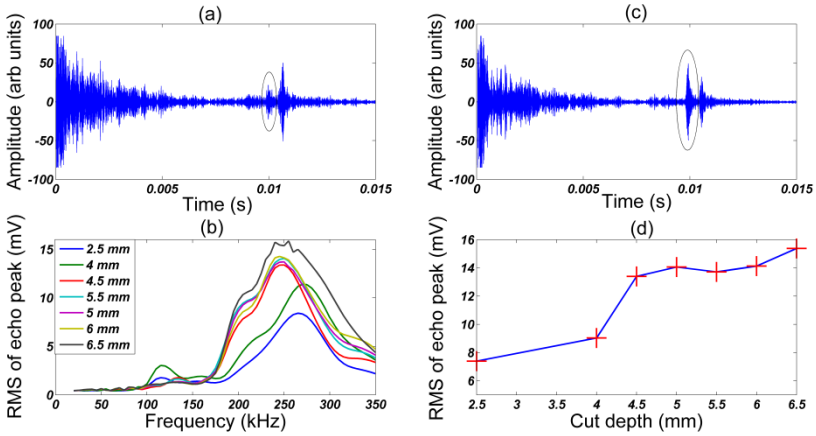

Figure 3-14 Graphs of (a) 260 kHz excitation response of 2.5 mm cut, (c) 250 kHz excitation response of 6.5 mm cut, (b) cut depth vs. reflection echo RMS vs. frequency and (d) cut depth vs. echo RMS information obtained at 250 kHz excitation. Defect echoes are circled in (a) and (c).

Figure 14(b) indicates that cut reflection echoes have their peak amplitudes at 250 kHz, which is in line with the results of previous section. Smaller cut depths, on the other hand, have their amplitude peaks at slightly higher frequencies (260-275 kHz range). A compromise for defect detection frequency identification, similar to previous part, is done based on the fact that four defect depths (4.5 to 6.5) have their peaks at the same frequency. Therefore, 250 kHz is chosen as the base frequency for the analysis of cut depth – echo RMS relationship, which is presented in Fig. 14(d). A quasi-linear relation, albeit sharper rates of change at smaller cut depths, can be observed in Fig. 14(d). Figure 14(a) and (c) show time domain representations of 2.5 mm cut and 6.5 mm cut at 260 and 250 kHz, respectively. 2.5 mm deep defect (4.5% reduction in CSA) is detected and 6.5 mm cut (30.7%) is also detectable. Moreover, far end resolution of defect detection is successfully lowered to 1.5 m.

Variations of frequencies where defects have their peak values suggest a dependence on defect size and type, a phenomenon also apparent in the previous section. In compliance with the frequency compromises mentioned in this section and the previous section, 250 kHz is accepted to be the best frequency for all defect types and sizes for accurate and long range defect detection.

3.8. :Critical Summary

A new defect detection system that utilises UGW is proposed for inspection of ACSR cables with aluminium layer inspection emphasis. A new transducer collar, formed of PZT transducers is designed and manufactured, and wave propagation in the cable is studied. Excitation frequencies between 200 and 300 kHz are reported to have good concentration of energy in aluminium layers, and present wave modes are shown to have similar group velocity dispersion curves with single-wire aluminium case. Defect detection using the fundamental longitudinal wave mode at an experimentally identified frequency (250 kHz) managed to detect defects corresponding to 4.5% reduction in CSA through a 26.5 metre long ACSR cable. A quasi-linear relation between defect depth and structural response is observed.

Although a good inspection range and defect detectability is achieved here even without post-processing, a better performance is still desirable. Towards this end, next chapter builds on the information presented in this chapter and uses the previously obtained data (in this chapter) for assessing various signal processing techniques for inspection range and signal quality improvements.

CHAPTER 4: Range/Signal Enhancement in UGW Testing of OVTL Cables

4.1. :Overview

In the previous chapter, even though 26.5 metre long cable is successfully covered and small defects are detected; received signals have long-duration dead zones and embedded noise. The noise observed in received signals, shown in Fig. III-13, could be coherent to transmit signal and could be caused by unwanted reflections caused by the air gaps and non-linear contact between individual wires. Alternatively, signals can be corrupted with non-coherent noise, such as measurement noise and noise generated by arbitrary sources. Aside from the fact that noise corruption can degrade defect detection quality, it can also reduce inspection range. In order to address these problems, certain signal processing algorithms are needed. Note that this chapter follows the experiments of the previous chapter, unless stated otherwise.

This chapter breaks the problem into two; improvement of SNR values of received signals and increasing the range of inspection. Firstly, wavelet transform based denoising techniques are proposed and its noise performance analysis is conducted for SNR improvement. Secondly, attenuation correction techniques, called time scaling throughout this thesis, are investigated for correcting the effects of attenuation to increase the inspection range. The combination of time scaling and wavelet denoising is also presented. Lastly, dispersion compensation techniques existing in the literature are coupled with time scaling to yield an extended range of inspection. Results yield remarkable SNR improvement for wavelet denoising (up to %24 percent), the feasibility of wavelet denoising and time scaling, and also a dramatic increase in inspection range in both cases (≈75 meters for time scaling and up to ≈130 meters for time scaling and dispersion compensation). Dispersion compensation and time scaling technique is also performed using narrow band tone bursts and broadband coded signals, both of which improved the resolvability of defects and increased the range of inspection. To the best of the author's knowledge, this is the longest inspection range for ACSR cables reported in the literature where typically only one or two meter long cables have been investigated previously.

4.2. :Introduction

Detection of defects in noisy environments, spatially overlapping echoes coming from closely spaced defects and the effects of dispersion phenomenon on wave propagation in interrogated media have been problematic for UGW applications, and raised the necessity of signal processing methods for inspection quality enhancement. Time – frequency analysis, deconvolution-based approaches, split spectrum processing, pulse compression **[69]**, sparse signal representations, empirical mode decomposition **[70]**, frequency warping **[71]** and wavelet transforms have been used for ultrasonic NDT applications **[72]**. Various studies have reported the use of advanced signal processing algorithms for the analysis of wave propagation and defect detection for multi-wire cables. Rizzo et al. utilised Discrete Wavelet Transform (DWT) to extract wavelet domain features for enhanced defect characterisation in

multi-wire strand structures **[73]**, and also reported the strength of DWT-based denoising in defect detection **[74]**. Wavelet transform is also utilised to achieve good time-frequency representation quality for defect detection in ACSR cables, as reported by Salazar et al. in **[75].**

Dispersion compensation techniques, where received time traces are compensated for the effects of dispersion, have attracted attention to compress received wave packets and to improve signal quality. Sicard *et al.* and Wilcox presented a method to compensate for the effect of dispersion from UGW signals in **[76]** and **[77].** Yamasaki *et al.* compared experimental and simulated time-reversed square pulses for dispersion compensation **[78].** They qualitatively showed that the technique can improve the SNR. However, no attempts have been made to extract the useful quantitative information such as ToF and propagation distance in multimodal response. Toiyama & Hayashi utilized PuC with dispersion compensation to enhance the SNR using chirp waveforms **[79].** However, the technique was only applied to single wave mode response and also no quantitative SNR improvement was presented. Marchi *et al.* combined PuC with Warped Frequency Transform (WFT) based dispersion compensation techniques in order to enhance the localization of the response of a steel cylindrical mass in an aluminum square plate **[80].** However, the technique requires wavelength filtering to suppress the effect of multimodal propagation. Zeng and Lin proposed a chirp-based dispersion pre-compensation technique using a priori knowledge of propagation distance **[81].** They concluded that the excitation waveform could be designed optimally to achieve a good resolvable resolution in order to extract the ToF of individual wave packets. However, in the case of heavily superposed wave packets (multimodal responses) this pre-processing technique may not be able to extract the accurate ToF. Also the application of the technique is restricted with manual intervention rather that an automatic computerized analysis. Xu *et al.* proposed a wideband dispersion reversal technique to self-compensate fundamental wave modes in a steel plate **[82].** They concluded that the synthesized Wideband Dispersion Reversal (WDR) signals can be used to simulate the pulse-like single wave mode packets which facilitate the wave mode identification and signal interpretation. However, compared with the dispersion compensation techniques, WDR scan method requires experimental validation for multimodal design with selective excitation. Also, in order to implement the WDR technique the propagation distance should be known.

This chapter is structured as follows. In Section 3, wavelet denoising technique is proposed and applied on empirical signals. In Section 4, time scaling concept is introduced and applied on signals obtained in previous chapter. Section 5 includes a thorough analysis of combined time scaling- dispersion compensation technique using excitation signals having various bandwidths.

4.3. :Wavelet Denoising

The wavelet denoising technique, which can be summarised as; *(a) wavelet transform (b) thresholding and (c) inverse wavelet transform* **[83]**, has an efficiency that depends on correct selection of parameters, such as mother wavelet, decomposition levels, thresholding algorithm and threshold value selection. In this study, continuous wavelet transform-based denoising is used.

Choice of mother wavelet should be made in accordance with the correlation between the mother wavelet and the echo reflection. Mother wavelets of Daubechies class, db40 and db6, are reported to perform well due to their good correlation with the ultrasonic reflection echoes in various structures **[74, 84],** though it is highly dependent on structure of interest. In this study, the mother wavelet was chosen based on its ability to detect the smallest defect (2.5 mm cut). Among various mother wavelets that are analysed, db45 mother wavelet with 5 decomposition levels yielded the best result, with hard thresholding scheme and fixed form (universal) thresholding selection rule. Figure 1 shows the results obtained using wavelet denoising for smallest cut depths, 2.5 and 4 mm, at respective peak frequencies (260 and 275 kHz).

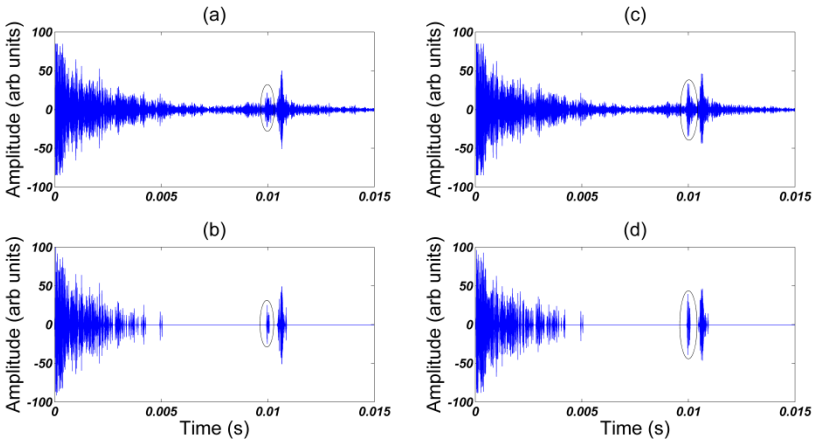

Figure 4-1 Graphs show the time traces obtained for 260 kHz excitation response of 2.5 mm cut (a) original and (b) wavelet denoised; time traces obtained for 275 kHz excitation response of 4 mm cut (c) original and (d) wavelet denoised. Defect echoes are circled in all subplots.

Proposed parameter selection for wavelet denoising successfully picked up the defect echoes for two smallest cut depths. Detection of these small defects indicates that deeper cuts would be detected as well, since deeper cut echoes would ideally have the same correlation with the chosen mother wavelet (unless defect orientation or type is different). Thus, two smallest cut depth signals are chosen for illustration in Fig. 15. In addition the cases shown in Fig. 1, the above mentioned wavelet denoising parameters managed to detect defects of varying depth and also denoised the signal.

Quantitative analysis of the performance of wavelet denoising is performed via SNR calculations. SNR is defined for the signal $\boldsymbol{x(t)}$ as **[84],**

$$SNR = \frac{Peak_{Defect\ Echo}}{\sigma_{\tilde{x}(t)}} \qquad \textbf{4.1}$$

where σ is the standard deviation. $\tilde{x}(t)$ (signal without deadzone) is defined as,

$$\tilde{x}(t) = \begin{cases} 0, t < \tau \\ x(t \geq \tau), t \geq \tau \end{cases} \qquad \textbf{4.2}$$

where $\boldsymbol{\tau}$ represents the time limit of the dead zone defined within time interval [0, $\boldsymbol{\tau}$]. In this study, based on observations made on raw signals, oscillations up to $\boldsymbol{\tau = 3ms}$ are chosen to be the dead zone.

SNR values are calculated for all cut depths with and without wavelet denoising, and results are illustrated in Fig. 2(a). Performance of wavelet denoising technique under simulated noise is also studied with different Additive White Gaussian Noise (AWGN) levels. Signals are corrupted with -10, -5, -3, 0, 3, 5 and 10 dB AWGN and then denoised via wavelet denoising. The procedure is repeated one hundred times for each noise level and for each cut depth, and the success rate of defect detection is analysed using SNR values. Average SNR values are obtained after repetitive noise corruption and denoising process and results are illustrated in Fig. 2(b). An SNR threshold value is derived visually (based on time domain representation of signals) that represents the limit of detection of defects after wavelet denoising (i.e. values below the threshold means no detection and vice versa).

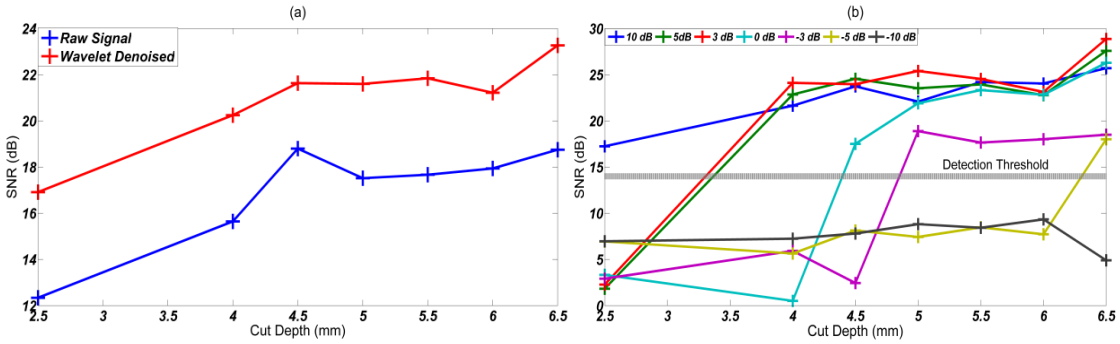

Figure 4-2 Graphs show SNR vs. cut depth for (a) original signals and (b) original signals corrupted by various levels of AWGN and then denoised via wavelet denoising. Grey horizontal line indicates the detection threshold.

Wavelet denoising, based on Fig. 2(a), consistently improves the SNR values of the signals where average improvement is around 4 to 6 dB (around 24% improvement). Results illustrated in Fig. 2(b) indicate that as the noise power increases, defects fall under noise level and they couldn't be detected. Small-depth defects fall under noise level quicker than deep defects and, therefore they become unresolvable easier (i.e. lower AWGN levels). For instance; the 260 kHz response of 2.5 mm cut, as shown in Fig. 2(b), can only be detected under the lowest AWGN level (10 dB). Relative to its depth, 6.5 mm cut can be detected with a higher AWGN level (-5 dB). Two representative results of denoising analysis, 260 kHz excitation response of 2.5 mm cut and 250 kHz excitation response of 6.5 mm cut, are illustrated in Fig. 3.

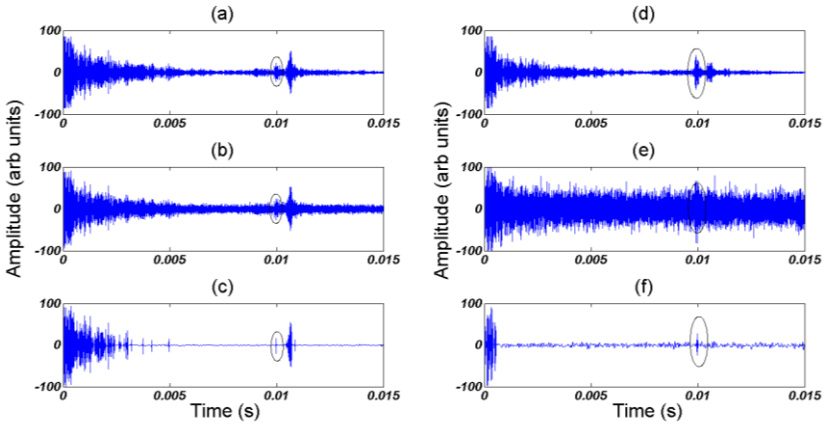

Figure 4-3 Graphs show the time traces obtained for 260 kHz excitation response of 2.5 mm cut (a) original, (b) under 10 dB AWGN and (c) under 10 dB AWGN and wavelet denoised; time traces obtained for 250 kHz excitation response of 6.5 mm cut (d) original, (e) under -5 dB AWGN and (f) under -5 dB AWGN and wavelet denoised. Defect echoes are circled in all subplots.

Figure 3(b) and (d) have some components that aren't filtered but have smaller wavelet coefficients than the defect. Ideally, the threshold value should be as close as possible to the defect's wavelet coefficient so that any component that has a lower coefficient falls under the threshold level and gets filtered. However, manual selection of thresholds with respect to the defect size isn't possible since that would require visual identification of defects and threshold value selection must be done accordingly. In this section, however, an automated technique managed to extract defects and improve signal SNR accordingly, albeit not efficient as a manual threshold selection would be.

Moreover, defects have remained detectable depending on their depth. It should also be kept in mind that in the case of ACSR cables, as mentioned earlier, coherent noise is quite severe. Therefore, additional noise would degrade signals more severely. Considering the length of the evaluated cable specimen and its respective attenuation, wavelet denoising performs adequately under additive noise.

4.4. :Time Scaling

UGW inspection range is often limited by the attenuation that the wave experiences as it propagates through the media. Time-Corrected Gain, where gain is increased with time, is a convenient way to address the attenuation problem. This, however, is limited by the available hardware.

An alternative approach is to use post processing to scale the received signal to correct for the effects of attenuation **[85].** Let $g(t)$ be a received signal sampled at time t. An exponential scaled version of this signal $y(t)$ can be calculated by

$$y(t) = g(t)\ e^{+\alpha\ t} \qquad \textbf{4.3}$$

where α is a positive constant that needs to be selected with respect to the attenuation experienced by the propagating wave.

The signals should be processed before being scaled to remove DC offset of the signal to prevent this being amplified by scaling operation. Figure 4 illustrates the results of time scaling technique applied on 275 kHz response of 4 mm cut signal, where α is set to 260**.**

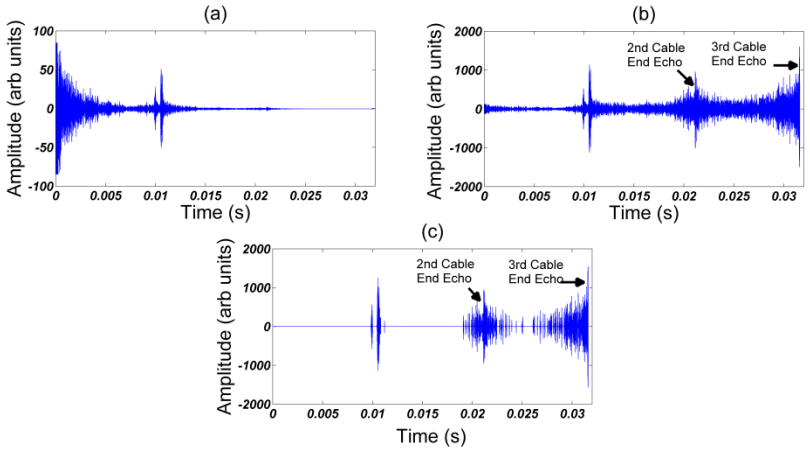

Figure 4-4 Graphs show the time traces obtained for 275 kHz excitation response of 4 mm cut (a) original, (b) time scaled and (c) time scaled and wavelet denoised .

In Fig. 4(a), a small echoes right after 0.02 s can be just seen. Using the group velocity of the longitudinal wave mode at 275 kHz, this small echo may be identified as the second echo from the cable end. After time scaling, illustrated in Fig. 4(b), the second and third cable end echoes become pronounced.
In Fig. 4(c), the time scaled signal is also denoised via wavelet denoising, using the same parameters in the previous sections, and a reasonable SNR improvement is visible. It can be seen in this figure that, although time scaling can correct for some effects of attenuation, it also has the effect of exponentially scaling the noise in the signal with time. In any case, though, seeing the third cable end echo indicates that inspection range is theoretically tripled and an ACSR cable of 78-metre length could in fact be inspected with the current hardware.

4.5. :Time Scaling and Dispersion Compensation

It is shown in previous sections of this chapter that the range of inspection is successfully increased three folds by time scaling, and separately, wavelet denoising managed to increase SNR value of received signals by up to 24%. Both techniques work considerably well together as well. However, a greater range of inspection is still desirable. Looking at the previous figures in this section, one may argue that received pulses from reflectors do not have single frequency component. This is expected since high frequency values are shown to be fruitful for long range inspection in ACSR cables, and although short duration tone bursts with Hann windows are used for excitation, excitation signals are likely to have a bandwidth. This bandwidth is expected to suffer from dispersion, since dispersion curves in this frequency band indicate dispersive characteristics for the wave mode used for excitation (L(0,1)).

Dispersion compensation techniques, however, require a priori knowledge of the dispersion curves of the medium. These are usually obtained, for structures such as pipes and plates, using commercial

software such as Disperse **[41]** or COMSOL **[86].** However, for ACSR cables, no software exists for generating dispersion curves for ACSR cables and it was considered to be difficult to achieve accurate results using modelling due to the complex geometry and unknown coupling between wire strands. As shown in the previous chapter, once the energy of the propagating wave is concentrated on the surface of the multi-wire structure, obtained dispersion curves are similar to that of the single wire case. Therefore, dispersion curves generated via Disperse is used to compensate for dispersion. The resulting dispersion curves were used to compensate three different experimental signals, which had different bandwidths.

4.5.1. :Wave Propagation Model and Dispersion Compensation

Although wave propagation is discussed briefly in the introduction chapter, a more generic formula of wave propagation as well as dispersion compensation is introduced here for clarity.

Assuming a signal h(t) excited by a transducer which propagates in M different wave modes will result in a signal g(t) after distance d can be written as

$$G(\omega) = \sum_{m=1}^{M} H(\omega) \exp(-[\alpha_m + jk_m(\omega)]d) + E(\omega) \quad \textbf{4.4}$$

where ω is the angular frequency, $H(\omega)$ is the Fourier transform of h(t), E is the noise, α_m and k_m are the attenuation coefficient and wave number for the m_{th} wave mode, respectively. Dispersion compensation for the m_{th} wave mode and the i_{th} propagation distance (or time) can be performed in the frequency domain by

$$Y_m(\omega, t_i) = G(\omega) \exp(\mathrm{j}[k_m(\omega)\mathrm{d}(t_i) - \omega t_i]) \quad \textbf{4.5}$$

where $\mathrm{d}(t_i)$ is the propagation distance calculated using

$$\mathrm{d}(t_i) = C_{gr}(\omega_{peak})t_i \quad \textbf{4.6}$$

where ω_{peak} is the group velocity of the frequency component that has the highest amplitude in the received signal $G(\omega)$. It must be noted that signal and time t_i would be shifted back to the origin in time axis, hence the term $t\omega_i$ for avoiding that. Once the dispersion compensation equation is converted back to the time domain by taking its Inverse Fourier Transform, one gets

$$\hat{y}(t) = IFFT\{Y_m(\omega, t_i)\} \quad \textbf{4.7}$$

This compensation procedure will theoretically provide the correct compensation of g(t) at time t_i , but will provide under or over dispersion compensation for other time instants. To overcome this, **(4.5)** and **(4.7)** are run in loop to cover all time instants. Resulting compensated signal is compensated for all times after this operation.

4.5.2. :Experimental Procedure

Experimental procedure adopted is similar to that of the previous chapter. However, all the experiments in this section are made using the 2nd deepest cut, which is 6 mm deep. Three types of transmit signals were used; 50 cycles of MLS white noise **[87]**, tone bursts, and Hann windowed tone bursts. These

transmit signal were chosen based on their different frequency bandwidths and hence different amounts of dispersion of the signal that occurs during propagation along the cable. MLS has a wide flat bandwidth (up to half of transmit sampling rate), while the Hann windowed tone burst signal has the narrowest bandwidth. The MLS was also chosen, as opposed to a chirp; because its frequency response is time independent making it more suitable for characterizing the wave propagation in the cable using spectrograms. It also has more power than a spike signal, such as a one or two cycle square wave. MLS signal is discussed in more detail in the next chapter.

4.5.3. :Dispersion Curve Acquisition and Wave Mode Identification

Although two different approaches are shown in the previous chapter with regards to the calculation of the dispersion curves, another one is made here using long duration experimental signals. 40-ms long recording has been made by exciting an MLS broadband pulse and then time scaling is applied. The spectrogram of the received signal is shown below.

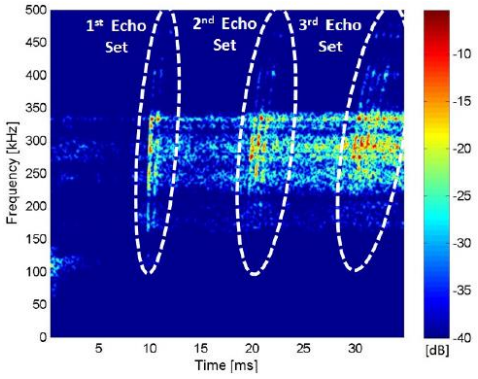

Figure 4-5 Spectrogram of the scaled time domain signal. Three sets of echoes can be seen in the data.

Figure 5 shows a spectrogram of the exponentially scaled signal obtained using MLS excitation. The echoes from the end of the cable and the adjacent cut can be seen as sets of curved lines (peaks) in the spectrogram at about 10, 20, and 30 ms. Since these curves have roughly the same shape, it appears that these are due to a single wave mode. The fact that these curves are increasingly deflected from the vertical with propagation distance means that this wave mode is experiencing dispersion. Recalling the information from the previous chapter, it seems that the only wave mode present in this recording is the fundamental longitudinal mode.

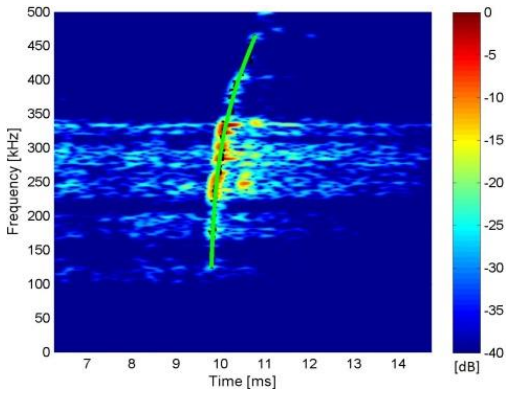

Figure 4-6 Spectrogram of a section of the received signal. The black dots show peaks obtained from this data for the first echo from the cut near the end of the cable. Fitted dispersion curve is then overlaid on this spectrogram (green).

A group velocity dispersion curve for the cable is measured by fitting peaks in the spectrogram data corresponding to echoes from the cut in the cable. A spectrogram is obtained of this data for the time period around the first echo. Peaks in the spectrogram data are then obtained in the frequency range where strong echo frequency components where present between approximately 115 and 450 kHz. A k^{th} nearest neighbor search is used to identify isolated peaks. These are regarded as noise and removed. Figure IV-6 shows the spectrogram with the denoised points and a fitted curve overlaid. This gives measurements of the arrival times $\tau(\omega)$ of the signal from the cut. Measured group velocities are then obtained by

$$C_{gr}(\omega) = \tau(\omega)/\,\mathrm{L} \qquad \textbf{4.8}$$

where L is the propagation distance along the length of the cable, which was twice the distance from the transducer array to the cut. Fitted dispersion curves, when adjusted for the helical length ratio, yields the group velocity dispersion curves (for aluminum) shown below.

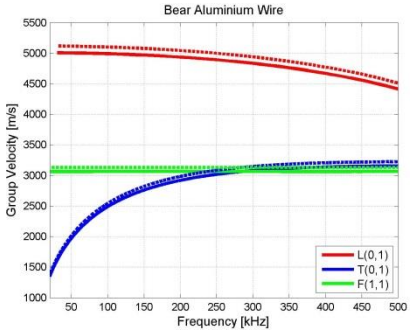

Figure 4-7 Original (dashed lines) and helical corrected (solid lines) theoretical group velocity dispersion curves for aluminum wires in the cable showing longitudinal L(0,1), torsional T(0,1), and flexural F(1,1) wave modes obtained using Disperse.

The helical twist effect produces a minimal variation for the values of the group velocity dispersion curves, though the trend of the curve doesn't change. Overlaying the above dispersion curves onto Figure IV-5 with the distance values shown in Table 1, following spectrogram is obtained.

Table 4-1 Table of distances used to calculate the arrival times for the three sets of echoes in Figure 8. The distances C and L are the distance from the array to cut and to the end of the cable, 25 and 26.5m, respectively.

Echo Set	Line 1	Line 2	Line 3	Line 4
1	2C	2L		
2	4C	2C + 2L	4L	
3	6C	4C + 2L	2C + 4L	6L

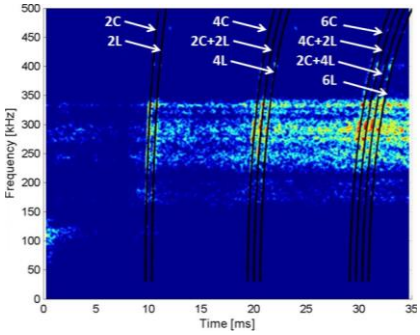

Figure 4-8 Spectrogram of the time scaled signal obtained using MLS excitation. Overlaid on top are the arrival times calculated using the propagation distances shown in Table 1 and the theoretical group velocity dispersion curve for the aluminum longitudinal wave mode.

As can be seen from Figure 8, there is a good agreement between the experimentally measured dispersion curves and the echoes, all of which propagate as the fundamental longitudinal wave mode.

4.5.4. :Dispersion Compensation Results

Figure 8 shows that, with time scaling, the echoes from defects in the cable show up clearly in the spectrograms for at least the first three echoes from the end of the cable. However, due to dispersion, these signals are spread out in the time domain resulting in reduced signal to noise ratio with propagation distance. In theory, dispersion compensation should be able to correct for this. This section looks at the effect of dispersion compensation of signal measured on the cable for MLS, tone burst, and Hann windowed tone burst signal.

4.5.4.1. :MLS Excitation

The dispersion compensation algorithm described in previous parts was applied to the time scaled signal obtained for MLS excitation, see Fig 8, using the theoretical dispersion curves obtained shown in Fig. 7. Figure 9 shows the resulting dispersion compensated signal. Figure 10 shows the Hilbert transform of the dispersed and dispersion compensated signals. An increase in SNR of between 4 and 8 dB is achieved. However, the main benefit is the fact that the individual echoes are able to be seen in the dispersion compensated signal which cannot be distinguished in the dispersed signal. The gain in ability to resolve individual peaks is from 7 to at least 13 dBs. A spectrogram of this dispersion compensated data is shown in Fig. 11 (a). It can be seen that the effect of the dispersion compensation was to make

the echo curves vertical in the spectrogram. An A-scan like time trace can be made from the spectrogram data. The spectrogram data which have units of dB, form an *MxN* matrix, where M is the number of frequencies and N is the number of times. A time trace signal in the form of a *1xN* vector can be achieved by summing down the columns (frequency components) of this matrix. Figure 11(b) shows the resulting trace for both the dispersed and dispersion compensated signal.

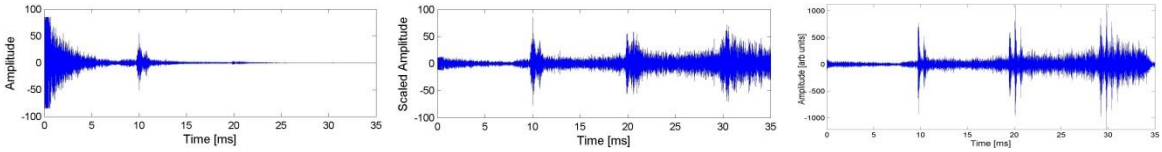

Figure 4-9 Plots of the time domain dispersed, time scaled, and time scaled-dispersion compensated signal (left to right).

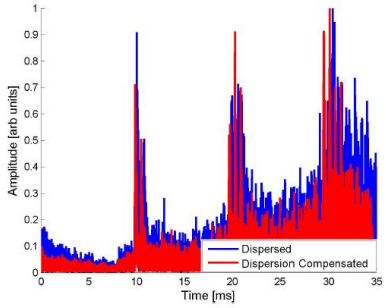

Figure 4-10 Plot showing the normalized Hilbert transform of the dispersed and dispersion compensated signals measured on the cables for MLS excitation signal.

Since the dispersion echo lines are not vertical in the spectrogram data, this technique gives blurred (dispersed) A-scan peaks for these echoes and a reduction in SNR with propagation distance. In contrast, the dispersion compensated signal is vertical in the spectrogram. This results in sharp peaks occurring for each individual echo and an increased SNR. It appears that dispersion compensation has the potential to increase the inspection range possible from a single location.

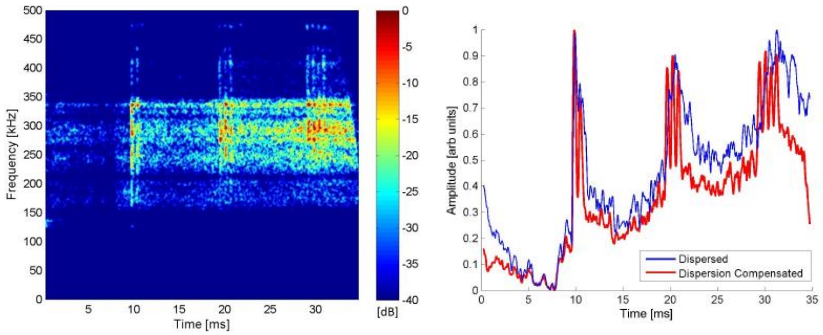

Figure 4-11 (a) Spectrogram of the dispersion compensated signal using MLS excitation, (b) trace obtained by summing the columns of the spectrogram data (units of dB).

To test the potential range that could be achieved using this technique, a longer recording of 60 ms was made for the MLS excitation signal. This was the longest recording able to be made using the data acquisition hardware. In an attempt to make the echoes less complicated for the longer recording, efforts were made to reduce the echoes from the cut. To achieve this, a metal band, plumbing clamp

was put over the cut and the transducer array was then moved to the same end of the cable as the cut. For this longer recording, the noise floor had a larger effect in the exponentially scaled signal.

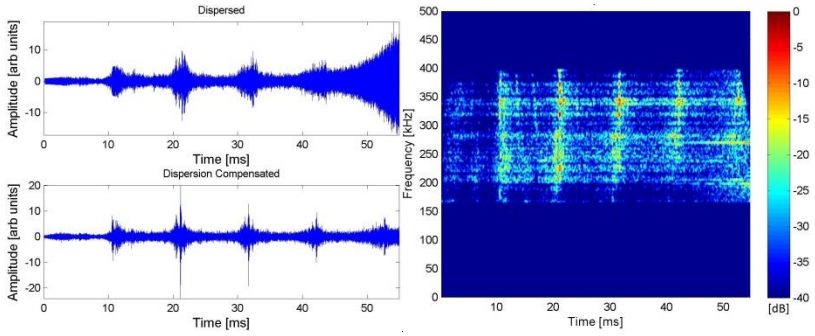

Figure 4-12 (a) Plots of the time domain dispersed and dispersion compensated-filtered signal for the long MLS recording, (b) Spectrogram of the dispersion compensated-filtered data (left to right).

This appeared as horizontal lines in the spectrogram which become exponentially scaled with increasing time. A possible source of these spectral lines was thought to be nearby switch mode power supplies. To reduce this, these noise spectral lines were manually identified and removed. Also, frequencies outside a frequency range of 160 to 400 kHz were also removed. Figure 12(a) shows the exponentially scaled and dispersion compensated signal. The echoes are sharper and there is an increased SNR for the dispersion compensated signal. Figure 12(b) shows the spectrogram of the dispersion compensated signal. The A-scans obtained from the spectrograms of the dispersed and undispersed signal is shown in Figure 13. The dispersion compensation had the effect of increasing the clarity of the echoes and increases the SNR compared to the dispersed signal. It can be seen that five echoes from the end of the cable can be seen with some weaker echoes from the covered cut. This theoretically corresponds to an inspection range of 130 meters. This shows that the combination of exponential scaling, dispersion compensation and filtering can effectively increase the inspection range for a broad band signal.

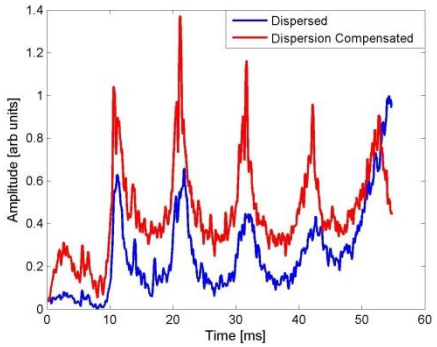

Figure 4-13 A-scan time trace of the dispersed and dispersion compensated signals.

4.5.4.2. :Narrow Bandwidth Signals

A main method used to address dispersion is to use a narrow bandwidth excitation signal. An example is a tone burst, which is a number of cycles of a sine wave. Although it has a central frequency, it has some bandwidth due to the low number of cycles which are typically used. To reduce this bandwidth, Hann

windowing of the tone burst signal is used. Therefore, tone burst and Hann windowed signal would be expected to experience different amounts of dispersion, which would be less than that experienced by the broadband MLS signal. Dispersion compensation was performed for these narrow band signals to see if a similar improvement in SNR could be achieved, as was observed for the broadband MLS signal.

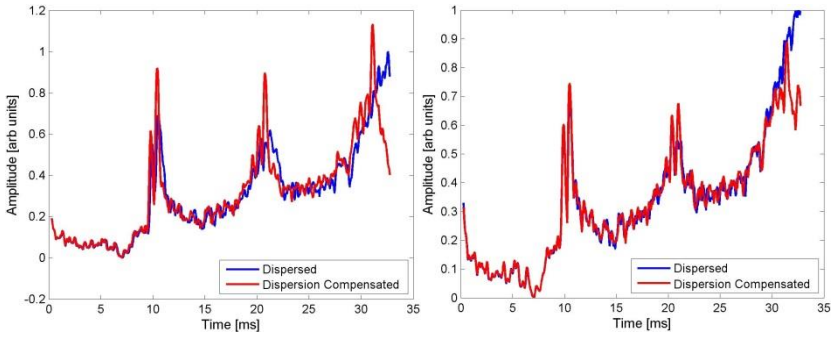

Figure 4-14 A-Scan of the dispersed and dispersion compensated signals obtained using a)tone burst excitation and b) Hann-windowed tone burst excitation, both of which are centered at 240 kHz and excited with 5-cycles (left to right).

Recordings were made using tone burst and Hann windowed, tone burst excitation signal with a transmit frequency of 240 kHz. The same experimental set up was used for these recordings. Dispersion compensation was then performed for these types of signal. Figure 14(a) and (b) shows the dispersed and dispersion compensated A-scans for the tone burst and Hann windowed tone burst excitation signal. It can be seen that an increase in SNR was achieved for both signals.

4.6. :Critical Summary

Following the work of the previous chapters, the limitation of inspection range and signal quality is investigated. Wavelet denoising, time scaling and dispersion compensation techniques are applied separately on signals obtained in the previous chapter's experimental setup. Wavelet denoising is applied to experimental signals and SNR improvement up to 24% is achieved. Wavelet denoising under additive noise is analysed. Time scaling technique is proposed and it successfully managed to increase inspection range approximately up to 78 meters. It is also shown that time-scaling and wavelet denoising works considerably well together. Lastly, time-scaling and dispersion compensation techniques are applied to further increase inspection range, both for broadband and narrowband signals. It was found that an increase in SNR of 4 to 8 dB was observed compared to the dispersed signal. However, the main benefit was an increased ability to resolution echoes from closely spaced structures; the end of the cable and an adjacent cut. Without dispersion compensation, only the first set of echoes could be clearly resolved. With dispersion compensation and some filtering, individual echoes could be distinguished clearly for at least five sets of echoes from the end of the cable. This would indicate an inspection range of up to 130 meters might be achievable. Dispersion compensation was also applied to narrow band signal and increased SNR and ability to resolution closely spaced echoes was obtained for these signals. While this study used an ACSR cable, this technique could be used for increasing the LRUT inspection range for other structures, such as plates, pipes, and other types of cables.

In addition to making advances towards having better signals (i.e. higher SNR) and extended inspection range, the defect localization problem is still not addressed. Next chapter takes a different route to address defect localization problem; it presents experimentations on a different structure that has superposed, multi-modal wave propagation (thus combatting a significantly more complex problem) and presents a novel signal processing algorithm that considers SNR improvement and defect localization.

CHAPTER 5: Automatic Defect Localization and Signal Improvement in UGW Testing

5.1. :Overview

In previous chapters, inspection range limitations and signal quality (defect detectability) problems are explained in detail and addressed. In UGW based NDT applications, there is another inherent problem; accurate localization of the structural discontinuity. Accurate localization of the discontinuity, in the context of NDT, means detecting where exactly the defect is in the structure. Localization quality is degraded due to several reasons; dispersion induced broadening of the echo coming from the reflector, failing to detect closely spaced defects due to signal duration and failing to detect defects due to low SNR.

This chapter attempts to address the localization problem in complex cases where there are multiple wave modes present. It is shown in previous chapter that in long range inspection of ACSR cables, due to frequency optimization and concentration of the wave energy on the surface wires, only fundamental longitudinal wave mode was present, and flexural wave mode attenuated quickly. Above mentioned scenario is relatively easy when it comes to complexity of the received signal as there is only one wave mode present. Here, the problem complexity is increased by evaluating a solid rod where multiple wave modes are present.

The problem of localization is combined with the aim of SNR improvement and a new technique comprising dispersion compensation and pulse compression is proposed. The technique is applied to the synthesized and experimental multimodal signals from an aluminum rod for performance verification. It is quantitatively validated that the technique noticeably improves the SNR of the guided wave response, and is able to derive an accurate time of flight of the individual wave modes and thus the propagation distance. The performance of the proposed technique using MLS is compared with the one given by chirp in the synthesis and experimentation. Noise analysis is also presented to further study the effectiveness of the technique for different excitation waveforms.

5.2. :Introduction

Dispersion problem and the ways to tackle it are discussed in previous sections. However, in the name of increasing localization accuracy, further steps are needed as even the dispersion compensated echoes might not have the required accuracy and might span several echoes, thus the low spatial resolution.

Pulse Compression (PuC) technique, where autocorrelation properties of certain coded waveforms are exploited, has found use in many applications such as medical ultrasound **[88]** and material

characterization **[89].** Due to its powerful SNR improvement and localization features, PuC technique has been widely used in air-coupled ultrasonic testing where acoustic impedance mismatch-induced SNR degradation severely limits the inspection quality. Gan *et al.* used capacitive transducers to generate chirp signals in air-coupled imaging of solid samples **[90**] and wood samples **[91]**; Rodriguez *et al.* used air-coupled piezoelectric arrays to utilize Golay codes to inspect copper plates **[92]** and Ricci *et al.* used chirp signals to inspect forged steels with high attenuation **[93].** Several studies have combined PuC with other techniques to further improve the SNR; Ricci *et al.* used chirp-based PuC combined with ℓ^1-norm total variation deconvolution **[94]** and Zhou *et al.* used wavelet transform to filter the noise and utilized Barker codes to perform PuC **[95].** Although PuC improves the SNR and localization, further improvements are still required in dispersive regions of the frequency spectrum since temporal broadening of the pulse still exists and limits the performance of PuC, hence the idea of combining dispersion compensation with pulse compression.

This thesis makes use of MLS to present an automated technique combining STFT, dispersion compensation and pulse compression. The performance of the technique using MLS is assessed and compared with the broadband chirp. It is shown that such a combination with cross-correlation can deliver SNR improvement and accurate extraction of ToF, thus the propagation distance simultaneously in a multimodal response.

The theoretical background is given in Section 3 and the proposed technique is described in Section 4. The technique is applied to synthesized and empirical MLS and chirp waveforms in Section 5 and 6, respectively. The performance of the technique using MLS and chirp is also quantitatively compared in Section 5 and 6.

5.3. :Theoretical Background

5.3.1.1. :Pulse Compression

PuC is a widely used technique for acquiring the impulse response of a system. For the proper exploitation of the technique, a signal with a good autocorrelation function ($ccf_{(x(t),x(t))} \cong \delta(t)$) is required **[91].** Signals satisfying desired autocorrelation condition that have been commonly used are linear/non-linear chirped sinusoids or pseudorandom binary sequences. Barker codes, MLS, Gold codes, Golay codes, Chaos sequence and Legendre sequence are examples of pseudorandom binary sequences used in the literature **[69].** In this thesis, MLS and linear chirp signals are used. Therefore, the next part provides brief information on MLS and chirp signals.

5.3.1.2. :Maximal Length Sequences

MLS are generated using Linear Feedback Shift Registers (LFSR) with N-delay taps, resulting in a sequence of length $\mathrm{L} = 2^N - 1$. More information about m-sequences can be found in **[96].** Autocorrelation function of an N-length m-sequence, an important feature exploited in this study, is given as,

$$ccf_{a,a}(t) = \begin{cases} 1, & lag = 0 \\ 1/N, & lag \neq 0 \end{cases} \quad \textbf{5.1}$$

In addition to its δ-function like autocorrelation function, m-sequences also have a flat spectral density with a near-zero DC component **[97].** In this thesis, MLS sequences are created using the work described in **[87].**

5.3.1.3. :Chirp Signals

Chirped sinusoids are broadband signals which could be created and tailored according to the frequency components desired in the signal. Chirp signals might have positive or negative chirp rates (*i.e.* frequency increases or decreases with time) and could have quadratic or linear characteristics. Since linear chirp signals are used in this study, a generic linear chirp equation is given below as,

$$x(t) = \sin(\Theta_0 + 2\pi(f_0 t + \frac{k}{2}t^2)) \quad \textbf{5.2}$$

where Θ_0 is the initial phase, f_0 is the starting frequency and k is the chirp rate, which is given as,

$$k = \frac{f_1 - f_0}{t_1} \quad \textbf{5.3}$$

where f_1 is the final frequency of the chirp and t_1 is the corresponding time of the final frequency.

5.4. :Proposed Technique

As mentioned in the previous section, UGW might experience dispersion as they propagate through a medium. A dispersed signal, as shown in **(4.4)**, could be compensated for dispersion via **(4.5)** which compensates for frequency-dependent velocities of the existing wave modes. The compensation process, however, requires *a priori* knowledge of propagation distance for accurate compensation, which makes it infeasible for real life applications especially where long range ultrasonic testing is of concern. A dispersion-compensated time trace would also have good SNR and good defect localization. However, in multi-modal scenarios where modes are superposed, the interpretation of received signals could be difficult. In such cases, PuC technique can be used to increase the ability to accurately locate defects as well as improve the SNR. For successful exploitation of the PuC technique, certain coded waveforms are considered.

Coded waveforms, such as chirped sinusoids and maximal length sequences, have δ-function like autocorrelation values which make them ideal candidates for source localization and SNR improvement. A received UGW, after it has been dispersion-compensated for correct propagation distance, denoted by $\tilde{x}(t)$, would ideally have good cross-correlation with the signal $x(t)$ excited from the transducer. Maximum value of cross correlation,$max\left(ccf\left(\tilde{x}(t), x(t)\right)\right)$, would provide accurate localization of the reflection echo, thus the structural discontinuity in the context of Ultrasonic NDT. An overall block diagram of the proposed technique is shown in Fig. 1.

The technique proposed in this study combines the dispersion-compensation technique described in **(4.5)** with the PuC technique in a brute-search manner$(h_{d(1)}(t),\ldots, h_{d(n)}(t))$. The dispersed (received

raw) signal $\tilde{x}(t)$ is iteratively compensated for dispersion for a range of propagation distances $(d(1), \ldots, d(n))$ and cross-correlated with the excitation signal. In every iteration, the maximum value of cross correlation ($c_{d(1)},\ldots,c_{d(n)}$) between the dispersion compensated signal and the excitation signal are stored with its respective propagation distance value. Once the iterative search is completed, stored max(ccf) values can be analyzed for various distances. After the maximum value of the stored max(ccf) values is extracted, the corresponding distance value of this maximum will provide the propagation distance (*d(i)*). Such analysis would also remove the need for *a priori* knowledge on the propagation distance for accurate dispersion compensation. This technique would provide robustness against noise and the interference of other wave modes.

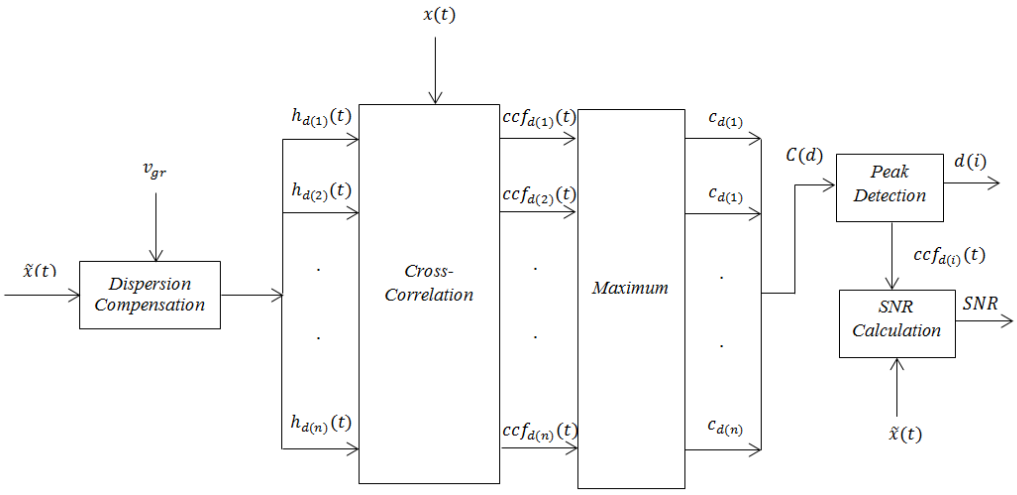

Figure 5-1 Block diagram of the proposed technique.

5.5. :Signal Modelling

The proposed technique is first analyzed with synthesized signals. The first signal considered was a 500-sample linear positive chirp sampled at 1 MHz that has frequency components between 10 to 125 kHz.

A constant appropriate sampling rate is used for the chirp signal **[98]** which satisfies the Nyquist criterion for the highest frequency/bandwidth acquisition. The MLS however needs to be sampled with a sampling rate of at least twice the highest desired frequency component of the signal **[97].** Therefore, to have a fair comparison with the chirp, both in terms of signal duration and frequency components, a 125-sample MLS signal was sampled with 250 kHz, which results in a signal that has time-invariant broadband frequency components up to 125 kHz. Signals are illustrated in Fig. 2 with their respective autocorrelation functions.

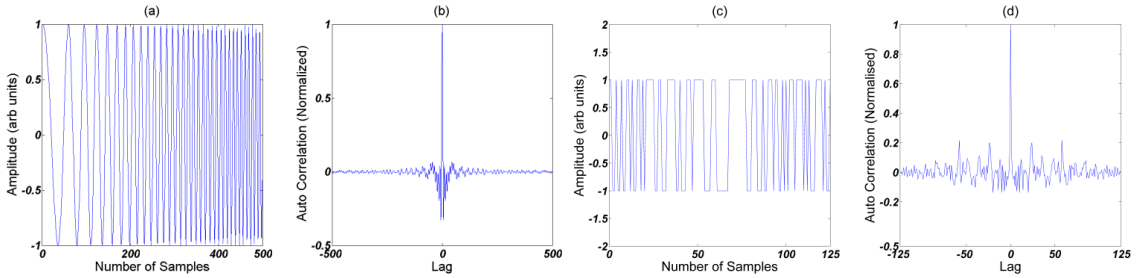

Figure 5-2 Synthesized chirp signal in (a) time domain and (b) its auto correlation; synthesized MLS signal in (c) time domain and (d) its auto correlation.

Dispersion simulations are performed for an aluminum cylindrical solid rod of 8-mm diameter. Group velocity dispersion curves for each wave mode propagating through the structure are acquired using Disperse **[41]** and shown in Fig. 3. L(0,1) and F(1,1) wave modes are considered for the signal modelling.

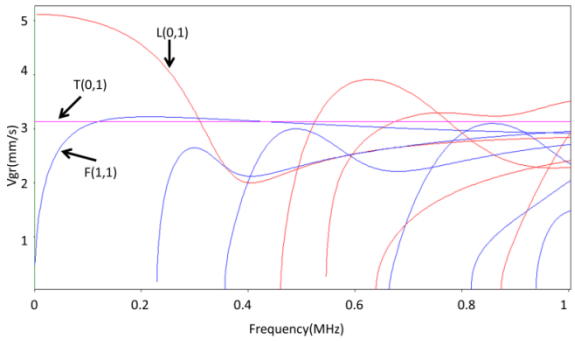

Figure 5-3 Group velocity dispersion curves of an aluminum rod of 8mm diameter. The fundamental modes are shown by arrows; higher order flexural and longitudinal modes are shown in blue and red, respectively.

5.5.1.1. :Single Wave Mode

Firstly, a relatively simple case, where only one wave mode is present, is considered. In the low frequency range (<200 kHz), due to its highly dispersive behavior, the fundamental flexural wave mode is chosen as the wave mode that the proposed technique would be applied on. Excitation signals are dispersed synthetically assuming a traveled path of 4.3 meters. Mode and frequency dependent attenuation is ignored.

Plots illustrated in Fig. 4(a) and (c) show dispersed signals' spectrograms. Overlaid curves are theoretical arrival time curves (black dots) which are calculated by dividing the distance (4.3 m) by the group velocity dispersion curve of fundamental flexural mode. Time-frequency representation of MLS is in good agreement with the overlaid dispersion curves due to its time-invariant broadband nature. Chirp, on the other hand, is broadband too yet its dominant frequency varies with time; therefore there is a misalignment between the dispersion curve and spectrogram of the chirp. Fig. 4(b) and (d) show the spectrogram of successful compensation (for 4.3 m) for the correct propagation distance for chirp and MLS. An important point here is the frequency that the dispersion compensation is based on; 48 kHz is chosen as the point of origin for dispersion compensation in this synthesis as this frequency had the peak in experimental signals assessed in Section 6. The slight difference of time-of-flight in dispersed and compensated signals' spectrograms seen in (Fig. 4) can be explained by the center frequency f_c. This

wouldn't change the propagation distance information since group velocity dispersion curves provide necessary information on wave velocity for each frequency value.

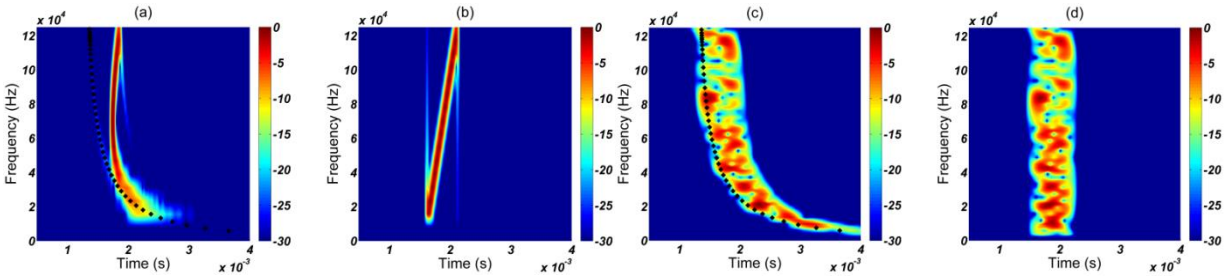

Figure 5-4 Spectrograms of synthesized unimodal signals with fundamental flexural Vgr dispersion curve (black dotted lines) overlaid; (a) linear chirp (dispersed for 4.3 m distance) and (b) dispersion compensated linear chirp; (c) MLS (dispersed for 4.3 m distance) and (d) dispersion compensated MLS.

The proposed iterative search technique is applied on artificially dispersed signals for a variety of distances ranging from 0 to 10 m with a step size of 0.01 m. Maximum cross-correlation values (as a function of distance) are normalized to their peak value and shown in Fig. 5(b) and (d), for chirp and MLS excitations, respectively. Both chirp and MLS excitation have successfully managed to extract the correct propagation distance (4.3 meters) without any errors.

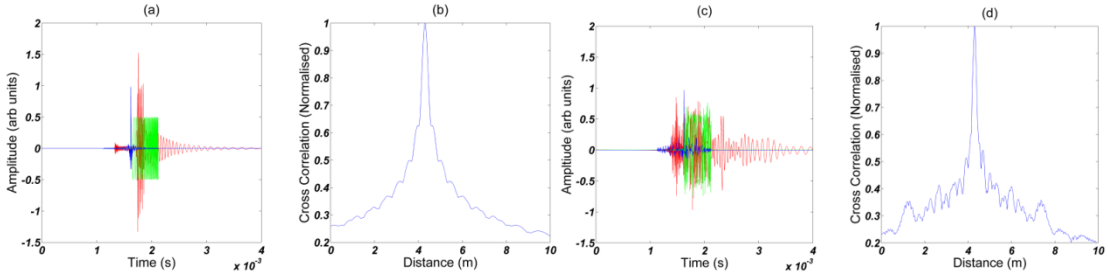

Figure 5-5 Unimodal synthesis results for the proposed technique; (a) dispersed (for 4.3 meters) chirp (red), compensated (green), normalized cross-correlation (blue) between dispersed and compensated signal, (b) chirp signal's maximum cross correlation (normalized to its peak value) trace as a function of distance, (c) dispersed (for 4.3 meters) MLS (red), compensated (green), normalized cross-correlation (blue) between dispersed and compensated signal, (d) MLS signal's maximum cross correlation (normalized to its peak value) trace as a function of distance**.**

Fig. 5(a) and (c) show the dispersed signal, dispersion compensated signal (for correct propagation distance) and successful compression of dispersion compensated pulse via cross correlation for chirp and MLS excitations, respectively. In addition to accurate acquisition of propagation distance, considerable SNR improvement can be observed by comparing the two signals shown in Fig. 5(a) and (c). SNR values in this study are calculated using **(4.1).**

Quantification of the SNR improvement is desirable for the wave mode of interest (*i.e.* the flexural wave mode since the iterative technique is applied on this mode). Therefore, $Peak_{Echo}$ value is chosen as the peak of the wave packet which corresponds to the wave mode of interest. Results of the SNR improvement are given in Table 1. It can be seen that MLS achieved 13.4 dB improvement whereas chirp achieved 10 dB improvement based on the flexural wave mode. The reason for the relatively low improvement of chirp SNR can be observed in Fig. 5(a) and Fig. 4(a). Since the gradient of the flexural

mode's dispersion curve and the chirp rate has different signs; chirp actually self-compensates during propagation, albeit not fully.

Therefore, there are high peaks observed in Fig. 5(a), which leads to a lower SNR improvement. MLS, on the other hand, has a time invariant frequency response; therefore dispersed signal is not compensated during propagation. This leads to a higher SNR improvement for MLS compared to chirp. However, it must be noted that the resulting SNR value of chirp is approximately 5 dB higher than the MLS signal.

5.5.1.2. :Multiple Wave Modes

In this section, a more complex case, where two superposed wave modes are present, is considered. In addition to the fundamental flexural wave mode, the fundamental longitudinal mode is also taken into account. The same excitation signals (used in previous part) are artificially dispersed assuming a travelled path of 4.3 meters for the flexural wave mode and 8.6 meters for the longitudinal wave mode, then individual wave modes are summed up. It can be calculated from Fig. 3 that above mentioned travelled path distances for the wave modes will result into a complex signal where two wave modes are superposed. Mode and frequency dependent attenuation is ignored.

The center frequency for dispersion compensation is chosen as 48 kHz. Dispersion compensation is performed on the flexural wave mode assuming a travelled path of 4.3 meters. Fig. 6(a) and (c) shows the spectrograms of dispersed signals for chirp and MLS excitations, respectively. Plots shown in Fig. 6(b) and (d) show the dispersion compensated (for 4.3 m) time traces for chirp and MLS excitations; it is evident that the first wave packets (the flexural wave modes) are compensated for dispersion accurately whereas the second wave packets (the longitudinal wave modes) are further dispersed since two wave modes have different dispersion curves.

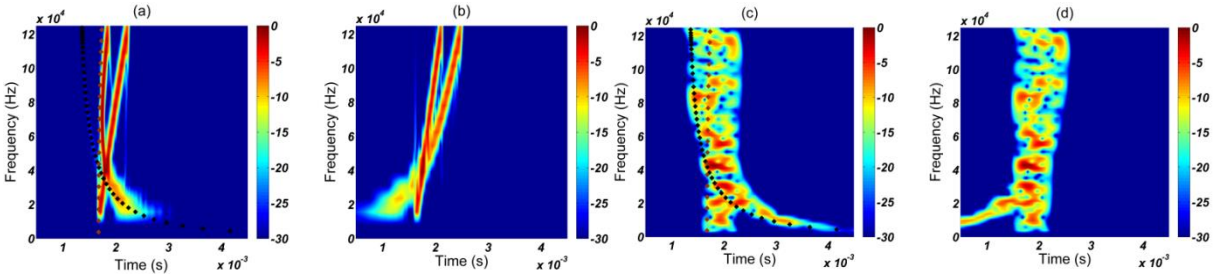

Figure 5-6 Spectrograms of synthesized multi-modal signals with fundamental flexural (black dotted lines) and longitudinal (brown dotted lines) Vgr dispersion curve overlaid; (a) linear chirp (dispersed 4.3 m for flexural and 8.6 m for longitudinal) and (b) dispersion compensated linear chirp; (c) MLS (dispersed 4.3 m for flexural and 8.6 m for longitudinal) and (d) dispersion compensated MLS.

The iterative search technique is applied on the above mentioned signals for a range of distances between 0 to 10 m with a step size of 0.01 m. Maximum cross correlation values, as a function of distance, are normalized (to their peak value) and shown in Fig. 7(b) and (d) for chirp and MLS excitations. Although the non-dispersive longitudinal wave mode provided high cross correlation values for all distances, the iterative technique still managed to extract the correct distance when compensating for the flexural wave mode for both the chirp and MLS signals. Fig. 7(a) and (c) shows the dispersed signal, compensated signal (for correct propagation distance) and cross correlation of the

excitation and compensated signals for chirp and MLS excitations. Multimodal time traces are successfully compressed (based on the flexural mode). Quantification of the SNR improvement for multimodal signals can be seen in Table 1.

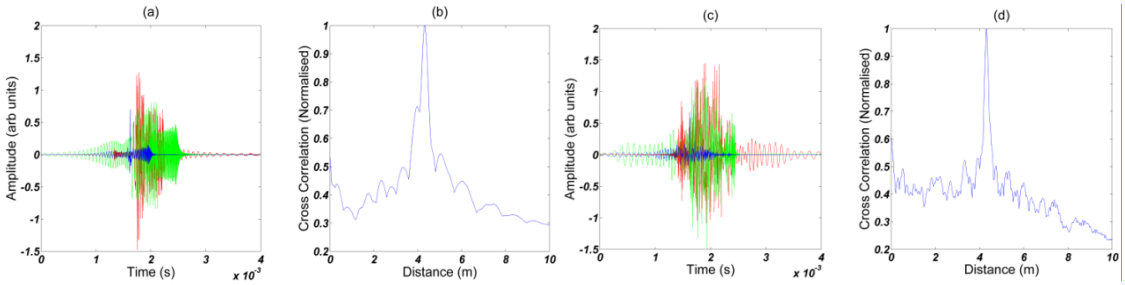

Figure 5-7 Multimodal synthesis results for the proposed technique; (a) dispersed (dispersed 4.3 m for flexural and 8.6 m for longitudinal) chirp (red), compensated (green), normalized cross-correlation (blue) between dispersed and compensated signal, (b) chirp signal's maximum cross correlation (normalized to its peak value) trace as a function of distance, (c) dispersed (dispersed 4.3 m for flexural and 8.6 m for longitudinal) MLS (red), compensated (green), normalized cross-correlation (blue) between dispersed and compensated signal, (d) MLS signal's maximum cross correlation (normalized to its peak value) trace as a function of distance.

Similar to the single wave mode synthesis, SNR improvement for the MLS signal is slightly higher than the chirp's SNR improvement (which is 13.5 and 11.7 dB, respectively). As was in the single mode synthesis, chirp is fairly self-compensated for dispersion and it has a higher peak in the first wave packet (which corresponds to flexural wave mode). Even though the received signal is more complex due to the second wave mode's interference, the MLS signal retains its high SNR improvement. However, similar to the single mode synthesis, it must be noted that the resulting SNR value of chirp is approximately 5 dB higher than the MLS signal.

5.6. :Experimentation

5.6.1.1. :Experimental Setup

Experimental verification of the proposed technique is performed on an aluminum cylindrical rod that was considered for simulations in Section 5. The length of the structure was 2.15 meters and a shear-mode lead zirconium Titanate (PZT) transducer was attached to one end of the rod with a clamp. The clamping configuration was adjusted so that the force was applied uniformly to the transducer. The structure was interrogated in pulse-echo configuration. A Teletest Unit **[65]** was used to drive the transducer. Power gain levels were fixed to 10dB. The analog input sampling rate was set to 1 MHz. The received signals were not averaged deliberately in order to consider a challenging scenario in terms of the measurement noise. The received signals were transferred to a PC for analysis in MATLAB. A representative diagram of the experimental setup is illustrated in Fig. 8.

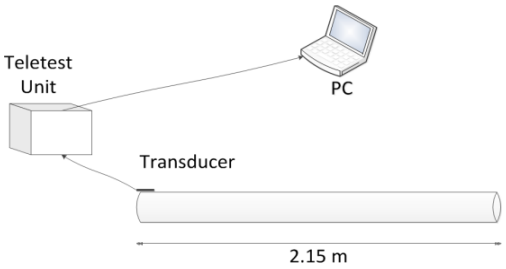

Figure 5-8 Representative diagram for the experimental setup.

In this section, the received signals and the excitation signals (both for chirp and MLS), prior to being fed to the proposed algorithm, were normalized via ℓ^2-normalization. This normalization is performed to map both signals into a comparable level in terms of power in case transducer output had fluctuations.

The excitation signals were chosen as a 65-sample MLS sampled at 250 kHz and a 250-sample positive linear chirp sampled at 1 MHz that has frequency components between 10 and 125 kHz. These signals are in line with the signals used in the synthesis part in terms of the signal durations and the frequency components. The duration of the chirp and MLS excitation signals were also approximately the same (0.26 and 0.25ms, respectively).

It must be noted that the excitation signals will be affected by the transfer function of the hardware and the transducer itself. These effects might lead to deterioration of the cross correlation and dispersion compensation steps of the proposed algorithm **[69].** A thorough analysis of electrical and mechanical resonance dynamics of the type of transducer used in this thesis can be found in **[99].** In the previous reference, it was reported that these types of transducers have a sufficiently flat frequency response in the frequency range of concern.

5.6.1.2. :Experimental Results

Signals fed from the hardware to the transducers are recorded both for the chirp and MLS excitations. These signals are illustrated in Fig. 9(a) and (c), with their autocorrelation properties shown in Fig. 9(b) and (d). The signal shapes are close to the synthesized waveforms shown in Fig. 2, and the autocorrelation results satisfy a δ-function like response. This verifies that the hardware system have good response in the frequency range of interest. Depending on the length of the rod and duration of the received signal, there can be multiple echoes and also multiple wave modes. In order to make it easier to demonstrate the technique, the received signals are windowed to acquire a certain window of time which corresponds to only two echoes.

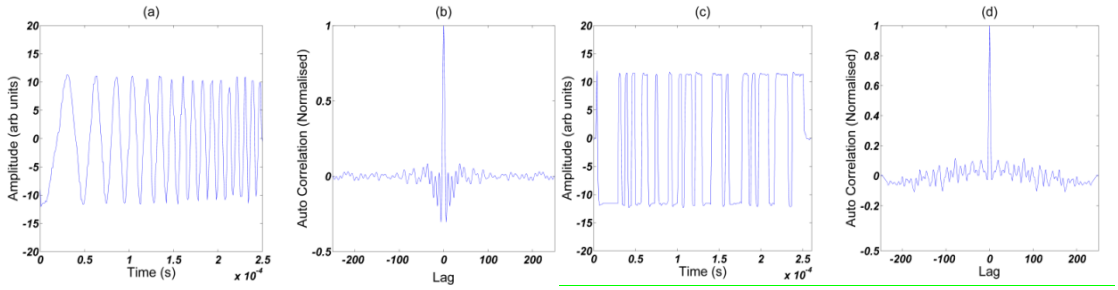

Figure 5-9 Plot of the chirp signal fed to the transducer in (a) time domain and (b) its auto correlation; plot of the MLS signal fed to the transducer in (c) time domain and (d) its auto correlation.

Spectrograms of the received signals for chirp and MLS excitations are shown in Fig. 10(a) and (c). The overlaid dispersion curves verify that the windowed signals consist of the second echo of the fundamental longitudinal mode and the first echo of the fundamental flexural mode. It can be seen that the modes are superposed especially in the low frequency region. The effect of this superposition can be seen in the spectrograms of the signals shown in Fig. 10. Due to the coupling of the transducer, the fundamental torsional wave mode is not excited. The center frequency for dispersion compensation is selected as 48 kHz. Also, in order to achieve accurate cross correlation results, only low frequency region of the received signals (<125 kHz, in line with excitation signal spectrums) are compensated. High frequency components of the signals, which were approximately 20 dB lower than the lower frequency regions, are ignored.

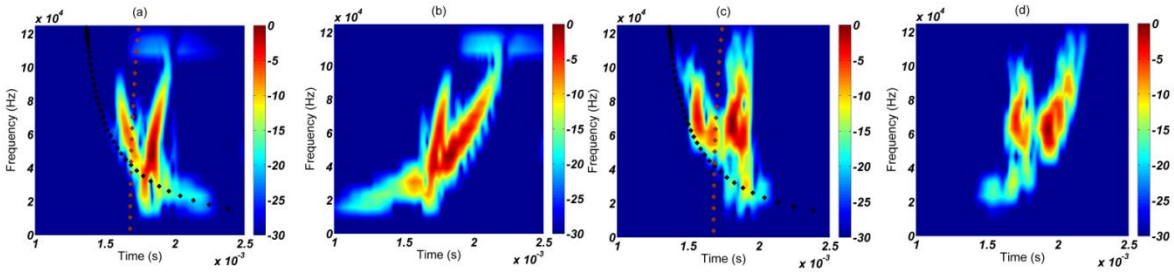

Figure 5-10 Measured signals' spectrograms with fundamental flexural (black dotted lines) and longitudinal (brown dotted lines) Vgr dispersion curve overlaid. Shown plots are (a) linear chirp, (b) dispersion compensated linear chirp, (c) MLS and (d) dispersion compensated MLS. Two wave modes shown in (a) and (c) are the first echo of the fundamental flexural mode and the second echo of the fundamental longitudinal mode.

5.6.1.2.1. :Flexural Mode Compensation

Fig, 11(a-b-c) and (d-e-f) show dispersed (ℓ^2-normalized), compensated (for flexural wave mode and for 4.3 m distance) and compressed chirp and MLS signals, respectively. The MLS signal, after compensation, shows two distinct and compressed peaks which account for the flexural and longitudinal modes, respectively. The chirp signal, on the other hand, exhibits a temporally spreading behavior and wave modes can't be distinguished from each other. Following the dispersion compensation and cross correlation, as shown in Fig. 11(c) and (f), both signals visibly have better SNR values based on the flexural wave mode. Moreover, localization of structural discontinuities is also improved in both cases, as can be seen by the sharp peaks in compressed signal plots. Quantification of the SNR improvement for experimental signals can be seen in Table 1.

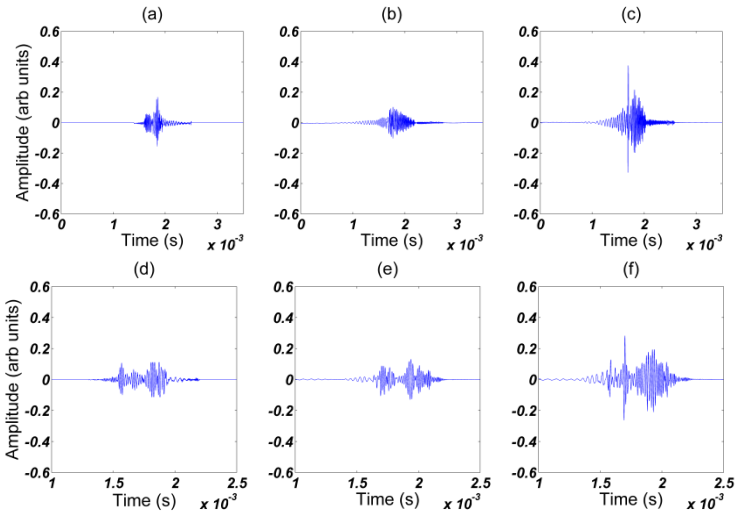

Figure 5-11 Plots show time domain representations of (a) measured chirp signal, (b) dispersion compensated (for 4.3 m) chirp signal and (c) cross-correlation between excitation and dispersion compensated chirp signal; (d) measured MLS signal, (e) dispersion compensated (for 4.3 m) MLS signal, and (f) cross-correlation between excitation and dispersion compensated MLS signal.

In the multimodal synthesis section, MLS had a higher SNR improvement compared to chirp. However, when combined with the measurement noise and structural response, SNR improvement of the MLS excitation is lowered. The SNR improvement for MLS is reported as 4.8 dB, whereas chirp retains its high SNR improvement, reported as 11 dB. Nevertheless, considerable SNR improvement is achieved for both signals.

The iterative search for the cross correlation maximum is performed for ranges between 0 and 10 meters with a step size of 0.01 m. Due to multi-modal nature of the signal (the longitudinal mode has high cross correlation with excitation signal since it has low dispersion) as well as the influence of the transducer and the hardware, cross-correlation values are high in short distances, as shown in Fig. 13. These high cross correlation values at short distances can be tackled by looking at the maximum cross correlation of the wave mode of interest (not the entire signal), however, that would require accurate spatial/temporal separation of two modes and that might not be possible when modes are superposed. Due to the above mentioned high cross correlation values in short distances, maximum of cross correlation traces (shown in Fig. 13) after a certain distance is taken into account and the maximum of the rest is taken. Based on the empirical findings, this distance threshold value is chosen as 1 meter since after 1 m, cross correlation maximums actually go below the peak observed at the correct propagation distance. Once the results of first meter are discarded, accurate results are obtained; 4.29 meter for MLS and 4.39 meter for chirp, which yields 0.01 m error for MLS and 0.09 m error for chirp. It must also be noted that results are within 0.01 m confidence level due to step size of distance (0.01 m).

5.6.1.2.2. :Longitudinal Mode Compensation

Even though the longitudinal wave mode has minimal dispersion in the windowed signal and this technique is proposed for dispersive wave modes, in order to achieve a complete analysis, the iterative

technique has been implemented on the experimental signals based on longitudinal wave mode compensation. All the parameters and signals used for the technique are the same with the previous section, except the dispersion compensation of the longitudinal wave mode. The results are shown in in Fig. 12.

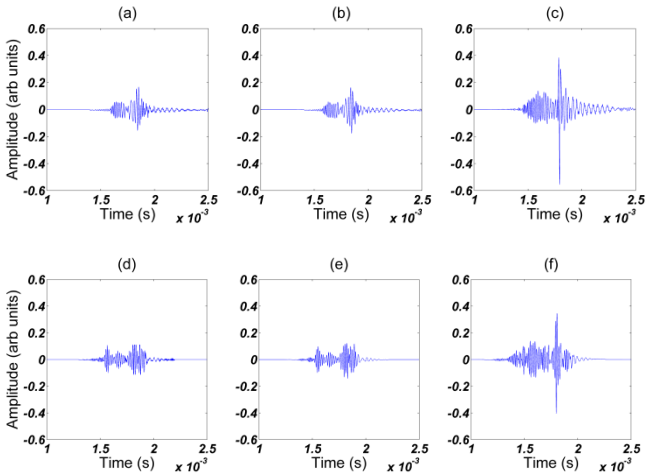

Figure 5-12 Plots show time domain representations of (a) measured chirp signal, (b) dispersion compensated (for 8.6 m) chirp signal and (c) cross-correlation between excitation and dispersion compensated chirp signal; (d) measured MLS signal, (e) dispersion compensated (for 8.6 m) MLS signal and (f) cross-correlation between excitation and dispersion compensated MLS signal.

Unlike the flexural-based compensation, the dispersed raw signals (Fig. 12 (a) and (d), same with Fig. 11 (a) and (d)) are approximately the same with the dispersion compensated (for 8.6 m, the propagation distance for longitudinal mode's second echo) signals illustrated in Fig. 12(b) and (e). This similarity is due to the non-dispersive nature of the longitudinal wave mode. Once the compensated signals are compressed using cross correlation, both chirp and MLS signals show distinct, sharp peaks for the second wave packet which is the longitudinal wave mode. Quantification of the SNR improvement for longitudinal-based compensation of experimental signals is given in Table 1.

In line with the previous results, MLS had a lower SNR improvement compared to chirp (5.5 and 7.5 dB, respectively). It must be noted that, since longitudinal is not dispersive, the initial peaks values are already high, as can be seen in Fig. 12(b-e). For an accurate analysis, the percentage increase of SNR values should be taken into account. The percentage improvement of MLS and chirp, reported as 24% and 39%, are lower than the flexural based compensation cases. Even though MLS improvement for flexural and longitudinal are really close, chirp had a dramatic decrease in the percentage SNR increase for longitudinal. It can, therefore, be said that the iterative technique based on longitudinal based compensation offers a good SNR improvement for both signals, albeit slightly worse than flexural based compensation.

In addition to the SNR improvement factor, the extraction of the propagation distance is also analyzed using the iterative method for longitudinal based compensation and the results are shown in Fig. 13. Compared to the flexural based compensation, the iterative method fails for the longitudinal based compensation in terms of extracting an accurate propagation distance for MLS and chirp signals. The peak values of the traces shown in Fig. 13 are different from the expected value (8.6 m). Another point

of interest is that there is minimal variation in the maximum cross-correlation peak with distance for the longitudinal mode. This is an expected phenomenon because the longitudinal mode experiences minimal dispersion and hence the iterative technique would yield similar results in terms of the cross correlation maximums for several distances. Even though, in an ideal situation, the peak value of the longitudinal-based compensation trace should give the correct propagation distance, the sensitivity to the noise as well as the frequency response of the medium indicate the iterative technique can't extract the correct propagation distance based on longitudinal mode compensation.

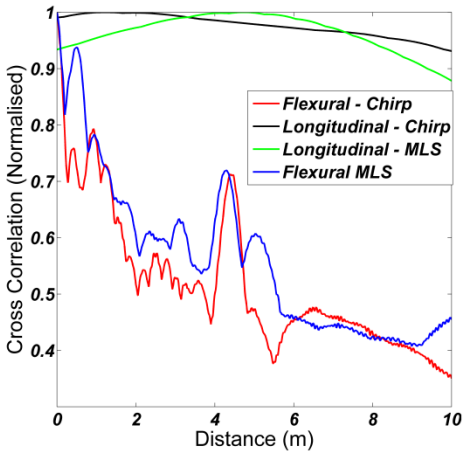

Figure 5-13 Plot shows the results of the iterative technique; maximum cross-correlation trace, as a function of distance, of experimentally received chirp (red) and MLS (blue) signals (compensation performed on flexural). Longitudinal- based compensation result are shown in black and green lines (chirp and MLS).

5.6.1.2.3. :Noise Performance

In addition to the complexity of signal interpretation introduced by multiple wave modes and hardware/transducer effect, experimental signals are also analyzed in degraded conditions via the introduction of Additive White Gaussian Noise (AWGN) of different levels (-20 to 20dB, with 5 dB steps). The noise addition procedure has been repeated hundred times for each noise level and proposed technique is then applied on noisy signals. In this section, only flexural based compensation is considered as the iterative technique couldn't yield good results in terms of propagation distance for longitudinal based compensation. Extracted propagation distance values are divided into four categories and defined in Algorithm 1. Results of the afore mentioned noisy signal detection classification are presented in Table 2 and 3.

Resulting propagation distance: *d, extracted propagation distance=d_x*
d_x =4.29 m for MLS, 4.39 for chirp
Success [1]: $d=d_x \pm 0.05m$ **10% Error [2]:** $d= d_x \pm 0.5m$
25% Error [3]: $d=d_x \pm 1\ m$ **>25% Error [4]:** $\begin{cases} d < dx - 1m \\ d > dx + 1m \end{cases}$

Algorithm 1: Noisy Signal Classification. Each class is numbered in brackets. These class numbers are used in the tables 2 and 3.

Detection performance of chirp and MLS vary under different noise levels. As expected, in high noise levels such as -20 dB, the percentage of the accurate results (Class 1 in Tables 1 and 2) obtained is really low. As the noise power decreases, number of accurate detections both for chirp and MLS excitations increase. However, as can be seen in Table 2 and 3, chirp excitation has a better performance in terms

of higher number of accurate detections as the noise power decreases. Under 0 dB noise, for instance, chirp has 52% accurate detection rate whereas MLS excitation has only 30%. The relatively low performance of MLS could be explained by its very nature; MLS is effectively a broadband white noise itself and this is likely to be vulnerable to noisy environments where noise can be modelled as White Gaussian Noise. Chirp, on other other hand, doesn't have a white noise-like characteristics, thus it can be argued that it is less vulnerable to AWGN. However, it must also be noted that nature of the noise is most likely to differ based on the environment, thus the relatively low performance of MLS presented here might not be indicative for every environment. Despite the fact that MLS performed slightly worse than chirp in high noise environments, as the noise power is lowered to 20 dB, both MLS and chirp excitations have around 90% accurate detection rates, which makes them feasible for this technique. It must be also noted that, as shown in Algorithm 1, extracted propagation distance for the chirp signal is already 0.08 m off than MLS.

5.6.1.2.4. :Remarks and Recommendations

The frequency response of the transducer and the hardware is an influential factor for the proposed iterative technique. As can be seen in Section 5 (multimodal synthesis), accurate propagation

Table 5-1 Table shows the SNR values for unimodal (single), multimodal (multi) and experimental (exp) signals for chirp and MLS excitations. SNR values are calculated using (7). Cases denoted by –L are longitudinal based compensation results, the rest are based on flexural mode compensation. Units are in dB scale. Raw columns are the SNR values of raw signals, result columns are resulting SNRs of compensated and then compressed pulses.

Case	Raw	Result	Increase	% Increase
Single Chirp	30.4805	40.5106	10.0301	32.91%
Single MLS	22.4023	35.7879	13.3856	59.75%
Multi Chirp	25.9025	37.6162	11.7137	45.22%
Multi MLS	19.2694	32.7846	13.4792	69.95%
Exp. Chirp	13.2812	24.4498	11.1686	84.09%
Exp. MLS	18.5787	23.4338	4.8552	26.13%
Exp. Chirp-L	18.9743	26.5613	7.5870	39.90%
Exp. MLS-L	22.4578	28.0050	5.5472	24.70%

Table 5-2 Table shows the detection rates (out of 100 repetitions) of the proposed technique (for flexural mode compensation) using experimental signals with various noise levels (-20 to 20 dB) for MLS excitation. Each column represents a noise power and each row represents a different classification. Class definitions are shown in Algorithm 1.

Class	-20	-15	-10	-5	0	5	10	15	20
1	1	7	5	12	30	36	58	87	94
2	17	17	27	33	47	48	64	87	94
3	28	31	29	33	47	48	64	87	94
4	72	69	71	67	53	52	36	13	6

Table 5-3 Table shows the detection rates (out of 100 repetitions) of the proposed technique (for flexural mode compensation) using experimental signals with various noise levels (-20 to 20 dB) for chirp excitation. Each column represents a noise power and each row represents a different classification. Class definitions are shown in Algorithm 1.

Class	-20	-15	-10	-5	0	5	10	15	20
1	2	11	22	41	52	59	61	83	89
2	13	28	49	75	89	99	100	100	100
3	24	36	49	75	89	99	100	100	100
4	76	74	51	25	11	0	0	0	0

distance results are obtained. However, due to measurement noise, transducer/hardware effect (even assumed in negligible levels) and the response of the structure, the frequency contents of the received signal were not the same as the excited signal. As a result, the extracted propagation distances had minor errors (Fig. 13).

The technique was also implemented with a lower distance increment (0.0001 m). It was observed for the experimental results that the technique had the same peak values at close distances, which means multiple maximum propagation distances were extracted. It can be argued that this depends on the resolution of the group velocity dispersion curve data used to compensate the signals for dispersion. In this thesis, the V_{gr} dispersion curve data was interpolated to cover a wide frequency range. This interpolation, however, could produce minor errors in certain frequencies' V_{gr} values. These minor errors might not be visible up to certain distance increment, yet it was visible in 0.0001 m distance increment resolution. The relatively insufficient resolution of V_{gr} data could also be presented as the reason of unsuccessful propagation distance extraction for the longitudinal mode presented in Section 6, as this wave mode is dispersed in a really minor way that V_{gr} data might not resolve.

5.7. :Critical Summary

In this chapter, the problem of defect localization and signal quality improvement are addressed in a combined manner. Dispersion compensation technique presented in previous sections is coupled with pulse compression using coded waveforms to improve SNR and localize defects by using two different coded waveforms; chirp and MLS.

The results given by MLS excitation were quantitatively assessed and compared with the chirp. Despite the existence of the measurement noise and superposed wave modes, the iterative search technique extracted an accurate propagation distance for MLS with 1 cm error which was superior to chirp with 9 cm error.

Moreover, considerable SNR improvement for both MLS and chirp (Table-1) was achieved. The technique was compared for different wave modes (dispersive flexural and non-dispersive longitudinal) in terms of the propagation distance extraction and the SNR improvement results. It was observed that SNR improvement can be achieved for both dispersive and non-dispersive wave modes, though the propagation distance extraction works accurately for the dispersive wave modes. The technique was

also analyzed with various levels of additive noise for both MLS and chirp (Table-2-3) based on empirically extracted propagation distances.

According to the signal synthesis and experimental results, MLS waveforms show promise for field inspection of cylindrical structures. The proposed technique also appears to be suitable when an automated system is required and long structures such as oil/gas pipelines are being examined.

Having presented all the material obtained in this research, next chapter concludes this thesis by highlighting the main contributions to the knowledge and drawing conclusions from the presented material. A guideline that contains future recommendations for researchers is also presented.

CHAPTER 6: Conclusions and Recommendations

6.1. :Main Findings and Conclusions

Research presented in this thesis reports several advances in NDT of power line cables, and also reports a new technique to be used out in the field for all guided wave applications. The general findings and associated conclusions of this research are listed below in chapter by chapter basis.

- **Chapter 3**

    - It is shown that only the fundamental longitudinal wave mode is suitable for long range defect detection as it propagates fast and it has minimal attenuation.
    - It is observed that by exciting high frequency ultrasounds in between 200 – 300 kHz, the energy can be concentrated on the outer wires of the cable, thus saving it from further attenuation. Less attenuation enables long range propagation of the wave, covering a longer distance (25 m) from what is reported in the literature
    - It is outlined that as the energy is concentrated on the surface wires of the cable via high frequency ultrasound, the propagating wave modes assume the properties that of a single-wire aluminum forming the outer layer of the cable. As the wires are twisted into a helical shape, one can obtain accurate dispersion curves by correcting the distance (that the wave propagates) with respect to the helical length ratio.
    - It is shown that 4.5% decrease in cross-sectional area can be detected through a 25 meter long ACSR cable just by frequency optimization without the need of any post processing.
    - It is also shown that any changes in cross sectional area, either positive or negative, can be detected by the system reliably.

- **Chapter 4**

    - It is shown that signals obtained in Chapter 3 can be further improved in terms of SNR by implementing wavelet denoising. Although dispersive and complex, the echoes coming from reflectors in ACSR cables can be picked up by correct selection of wavelet denoising parameters. These optimized parameters are empirically found and are listed

as an accomplishment of this thesis. Using the correct parameters, SNR values of varying defect sizes are improved. In the best case, up to 24% SNR improvement is achieved.

- Through the implementation of attenuation correction framework called time scaling, a theoretical three-fold increase (75 m) is achieved in inspection range. Moreover, it is also shown that time scaling could work well when combined with the wavelet denoising technique.

- Based on the observation of dispersiveness of the received signals, implementation of dispersion compensation combined with time scaling is presented. Combining the best of two aforementioned techniques, dispersion compensation and time scaling is shown to be capable of improving the SNR, as well increasing the inspection range dramatically up to 130 meters.

- It is also shown by combined dispersion compensation and time scaling technique that closely spaced defects can be resolved although in their raw format they weren't resolvable. This represents a huge improvement for not only guided wave inspection in power line cables, but for all guided wave based NDT applications.

- **Chapter 5**

  - A new technique is proposed which tackles the problem of signal quality and accurate localization of defects in structures.

  - The technique proposes the utilization of coded waveforms Maximal Length Sequences and chirped sinusoids. The technique, by iteratively compensating the received signals for dispersion and cross-correlating the compensated version to the excited signal, acquires the propagation distance within a good confidence interval, both for chirp and MLS
  - It is shown that Maximal Length Sequences are good candidates as coded waveforms to improve SNR of the signals. Such outcome gains strength through a comparison between MLS and chirp, one of the most common waveforms used in UGW based NDT applications.

- MLS also has the capability of presenting accurate information about the dispersion curve of the structure due to its time-invariant broadband feature. This technique can thus be used in material characterization as well.
- It is shown that dispersion compensations works better for wave modes that are highly dispersed. This is due to the resolution of the group velocity dispersion curve provided by commercially available software tools.

6.2. : Recommendations

In addition to the advances reported in the thesis, there are limitations of the reported techniques, as well as the limitations of the inspection of power line cables in general. Several recommendations to tackle those limitations are listed below.

- Although an inspection range of 130 meters is achieved, the experiments are done using a 26.5 meter long cable. Experimentations with longer cables are required to verify the results and validate them industrially.

- It is shown in the third chapter of the thesis that 200-300 kHz range provides fruitful results for long range inspection of power line cables. However, in these frequencies, satisfactory experimentations were not completed with regards to the detection of defects in the steel core. Although measurements performed in short range cables (reported in the ECNDT 2014 conference paper listed in the publications sections of the first chapter) indicate steel penetration in 200 – 300 kHz frequency range, it is not yet clear if longer range measurements lack the steel penetration because of the coupling of the transducer or simply the attenuation of the wave energy in the steel core. This is an interesting point to carry on with the research in author's opinion.

- Although not necessarily required, the overall experimentation could be done while power line cables are online. Since it contains health hazards, such experiments couldn't be completed during this research. However, the possible generation of ultrasound in the cable due to flowing high current might further increase complexity of the received signals in the systems. If such problem could be tackled, this will save the industry from downtime and dramatically increase the value of the system described in this thesis.

- Due to extremely complex and rather stochastic nature of the received signals, physics-based approaches can be replaced with data-driven approaches which implement pattern recognition techniques to identify and classify defects in power line cables. Moreover, such data-driven approaches are more likely to produce generalized techniques that can be used for various multi-wire cables, for which conventional signal processing might be insufficient as it is more

structure-specific. Lastly, such approaches have the potential to be highly robust against hostile environments; therefore they seem as a promising prospect for further research.

- As mentioned before in several parts of this thesis, presented research adopts an experimental pathway towards the analysis of UGW in OVTL cables. In-depth theoretical work to further build on various studies should be conducted to expand the existing theory to multi-wire cables. Achieving this would dramatically increase the efficiency of future techniques and would be beneficial to industrial and academic parties.

- It is evident from the state of the art that new UGW based inspection techniques are making use of more sophisticated signal processing algorithms that were initially developed for other fields such as radar signal processing and telecommunications. Future researchers are encouraged to take this pathway to enrich the literature of UGW based NDT.

CHAPTER 7: REFERENCES

[1] Van Hemelrijck, Danny, and Athanassios Anastassopoulos, *Non Destructive Testing*. CRC Press, 1996.
[2] Moon, Peter. "The Hartford Steam Boiler Inspection and Insurance Company."*Sci-Tech News* 49.2 (2013): 4.
[3] Valavanis, Ioannis, and Dimitrios Kosmopoulos. "Multiclass defect detection and classification in weld radiographic images using geometric and texture features." *Expert Systems with Applications* 37.12 (2010): 7606-7614.
[4]"Radiography in Modern Industry." *Kodak Company*. Kodak Company, 1 Jan. 1980. Web. 19 Jan. 2015. <http://www.kodak.com/eknec/documents/87/0900688a802b3c87/Radiography-in-Modern-Industry.pdf>.
[5] Zhigang Qu, M.K. Yucel, Alvin Yung Boon Chong, Juan Luis Ferrando Chacon, Vassilios Kappatos, Cem Selcuk, Tat-Hean Gan, "*Surface Weld Flaw Identification using Laser Triangulation Principle",* YPIC' 2014 Conference, 2014.
[6] Qi, Gang. "Wavelet-based AE characterization of composite materials." *NDT & E International* 33.3 (2000): 133-144.
[7] Chacon, Juan Luis Ferrando, et al. "Shaft angular misalignment detection using acoustic emission." *Applied Acoustics* 85 (2014): 12-22.
[8] Al-Ghamd, Abdullah M., and David Mba. "A comparative experimental study on the use of acoustic emission and vibration analysis for bearing defect identification and estimation of defect size." *Mechanical systems and signal processing* 20.7 (2006): 1537-1571.
[9] Mba, David, and Raj BKN Rao. "Development of Acoustic Emission Technology for Condition Monitoring and Diagnosis of Rotating Machines; Bearings, Pumps, Gearboxes, Engines and Rotating Structures." (2006).
[10] Sophian, Ali, et al. "Design of a pulsed eddy current sensor for detection of defects in aircraft lap-joints." *Sensors and Actuators A: Physical* 101.1 (2002): 92-98.
[11] He, Yunze, et al. "Pulsed eddy current imaging and frequency spectrum analysis for hidden defect nondestructive testing and evaluation." *Ndt & E International* 44.4 (2011): 344-352.
[12] Pohl, Rainer, et al. "NDT techniques for railroad wheel and gauge corner inspection." *NDT & E International* 37.2 (2004): 89-94.
[13] García-Martín, Javier, Jaime Gómez-Gil, and Ernesto Vázquez-Sánchez. "Non-destructive techniques based on eddy current testing." *Sensors* 11.3 (2011): 2525-2565.
[14] Dick, Paul. "Scanning Electron Microscope, A Valuable NDT Method." *NDT.net*. NDT.net. Web. 20 Jan. 2015. <http://www.ndt.net/article/wcndt00/papers/idn001/idn001.htm>.
[15] Sutton, Michael A., et al. "Scanning electron microscopy for quantitative small and large deformation measurements part I: SEM imaging at magnifications from 200 to 10,000." *Experimental mechanics* 47.6 (2007): 775-787.
[16] Gao, Shang-Lin, and Jang-Kyo Kim. "Scanning acoustic microscopy as a tool for quantitative characterisation of damage in CFRPs." *Composites science and technology* 59.3 (1999): 345-354.
[17] Clark, M. R., D. M. McCann, and M. C. Forde. "Application of infrared thermography to the non-destructive testing of concrete and masonry bridges."*Ndt & E International* 36.4 (2003): 265-275.

[18] Shih, J. K. C., et al. "Application of Infrared Thermography for Damage Detection in Structural Concrete– Preliminary Report." *NDT. net* 5.02 (2000).
[19] Ibarra-Castanedo, Clemente, et al. "Active infrared thermography techniques for the nondestructive testing of materials." *Chapter XIV of the book:"Ultrasonic and Advanced Methods for Nondestructive Testing and Material Characterization", ed. Chen CH* (2007): 325-348.
[20] N.P. Avdelidis et al., "Infrared thermography as a non-destructive tool for materials characterisation and assessment", Thermosense: Thermal Infrared Applications XXXIII, Orlanda, Florida, USA, April 2001.
[21] Lovejoy, David. *Magnetic Particle Inspection: A Practical Guide. David Lovejoy*. Springer Science & Business Media, 1993.
[22] Clapham, Lynann, Vijay Babbar, and James Byrne. "Detection of mechanical damage using the magnetic flux leakage technique." *2004 International Pipeline Conference*. American Society of Mechanical Engineers, 2004.
[23] Babbar, Vijay, James Bryne, and Lynann Clapham. "Mechanical damage detection using magnetic flux leakage tools: modeling the effect of dent geometry and stresses." *NDT & E International* 38.6 (2005): 471-477.
[24] Wang, Z. D., Y. Gu, and Y. S. Wang. "A review of three magnetic NDT technologies." *Journal of Magnetism and Magnetic Materials* 324.4 (2012): 382-388.
[25] Dover, W. D., et al. "Fitness for purpose using ACFM for crack detection and sizing and FACTS/FADS for analysis." *Marine Structural Inspection, Maintenance, and Monitoring Symposium*. 1991.
[26] Topp, D., and M. Smith. "Application of the ACFM inspection method to rail and rail vehicles." *Insight-Non-Destructive Testing and Condition Monitoring*47.6 (2005): 354-357.
[27] Krautkramer, Josef and Krautkramer, Herbert, Ultrasonic Testing of Materials, 4th/revised edition, Springer Verlag, November 1990, ISBN: 0387512314
[28] Cartz, Louis, Nondestructive Testing : Radiography, Ultrasonics, Liquid Penetrant, Magnetic Particle, Eddy Current, ASM Intl; ISBN: 0871705176
[29] Auld, B.A., Acoustic Fields and Waves in Solids, Vol I & II, 2nd edition Krieger Publishing Company, February 1990; ISBN: 089874783X
[30] B. A. Auld, Acoustic Fields and waves in solids, vol. 2. Krieger Publishing Company Malabar, 1990
[31] Lowe, Michael JS. "Matrix techniques for modeling ultrasonic waves in multilayered media." *Ultrasonics, Ferroelectrics, and Frequency Control, IEEE Transactions on* 42.4 (1995): 525-542.
[32] Strutt, John William, and Lord Rayleigh. "On waves propagated along the plane surface of an elastic solid." *Proceedings of the London Mathematical Society*17 (1885): 4-1.
[33] Bergman, R. H., and R. A. Shahbender. "Effect of statically applied stresses on the velocity of propagation of ultrasonic waves." *Journal of Applied Physics*29.12 (1958): 1736-1738.
[34] Lamb, Horace. "On waves in an elastic plate." *Proceedings of the Royal Society of London. Series A, Containing papers of a mathematical and physical character* (1917): 114-128.
[35] Pochhammer, Lt. "Ueber die Fortpflanzungsgeschwindigkeiten kleiner Schwingungen in einem unbegrenzten isotropen Kreiscylinder." *Journal für die reine und angewandte Mathematik* 81 (1876): 324-336.
[36] C. Chree, "The equations of an isotropic elastic solid in polar and cylindrical coordinates, their solution and applications," Trans. Cambridge. Philos. Soc., vol. 14, pp. 250{369, 1889

[37] Gazis, Denos C. "Three-Dimensional Investigation of the Propagation of Waves in Hollow Circular Cylinders. I. Analytical Foundation." *The journal of the Acoustical Society of America* 31.5 (1959): 568-573.
[38] Gazis, Denos C. "Three-Dimensional Investigation of the Propagation of Waves in Hollow Circular Cylinders. II. Numerical Results." *The Journal of the Acoustical Society of America* 31.5 (1959): 573-578.
[39] Silk, M. G., and K. F. Bainton. "The propagation in metal tubing of ultrasonic wave modes equivalent to Lamb waves." *Ultrasonics* 17.1 (1979): 11-19.
[40] Viktorov, Igor Aleksandrovich. *Rayleigh and Lamb waves: physical theory and applications*. Plenum press, 1970.
[41] Pavlakovic, B., and M. Lowe. "Disperse user manual: a system for generating dispersion curves." *Copyright B Pavlakovic, M Lowe* (2003).
[42] Chen, Guohong, et al. "Damage investigation of the aged aluminium cable steel reinforced (ACSR) conductors in a high-voltage transmission line." *Engineering Failure Analysis* 19 (2012): 13-21.
[43] Siegert, D., and P. Brevet. "Fatigue of stay cables inside end fittings: high frequencies of wind induced vibrations." *Bulletin-International Organisation for The Study of The Endurance of Ropes* 89 (2005): 43.
[44] Azevedo, C. R. F., and T. Cescon. "Failure analysis of aluminum cable steel reinforced (ACSR) conductor of the transmission line crossing the Parana River." *Engineering Failure Analysis* 9.6 (2002): 645-664.
[45] Shoemaker, Thomas M., and James E. Mack. *The lineman's and cableman's handbook*. McGraw-Hill, 2007.
[46] Stix, Gary. "Working hot: life at 765 kV." *Spectrum, IEEE* 25.9 (1988): 54-56.
[47] U.S. Helicopter summary statistics, Helicopter Association International, 1996-2004.
[48] Katrasnik, Jaka, Franjo Pernus, and Bostjan Likar. "A survey of mobile robots for distribution power line inspection." *Power Delivery, IEEE Transactions on*25.1 (2010): 485-493.
[49] Snell Jr, John R., and Joe Renowden. "Improving the results of thermographic inspections of electrical transmission and distribution lines." *AeroSense 2000*. International Society for Optics and Photonics, 2000.
[50] Sutton, J., and K. G. Lewis. "The Detection of Internal Corrosion in Steel-Reinforced Aluminium Overhead Power Line Conductors." *UK Corrosion*. Vol. 86. 1986.
[51] Linuma. I. et al. 1992. 'Corrosion Detector Robot for Overhead Transmission Line,' Fujikura Technical Review.
[52] Jiang, Xingliang, et al. "An S-Transform and Support Vector Machine (SVM)-Based Online Method for Diagnosing Broken Strands in Transmission Lines."*Energies* 4.9 (2011): 1278-1300.
[53] Kasinathan, M., et al."Fiber optic sensors for monitoring sodium circuits and power grid cables." *Advancements in Nuclear Instrumentation Measurement Methods and their Applications (ANIMMA), 2011 2nd International Conference on*. IEEE, 2011.
[54] Investigation of applying new technologies to overhead transmission line inspections, Project 1497–2, Electric Power Research Institute Report, September 1981.
[55] Jiang, Xu, et al. "Detecting the flaws in prestressing strands using guided waves based on the magnetostrictive effect." *Insight-Non-Destructive Testing and Condition Monitoring* 49.11 (2007): 647-650.

[56] Xu, Jiang, et al. "Broken wire detection in stay cables based on guided waves. *"Mechanic Automation and Control Engineering (MACE), 2010 International Conference on*. IEEE, 2010.
[57] Liu, Zenghua, et al. "Configuration optimization of magnetostrictive transducers for longitudinal guided wave inspection in seven-wire steel strands." *NDT & E International* 43.6 (2010): 484-492.
[58] Rizzo, P. "Ultrasonic wave propagation in progressively loaded multi-wire strands." *Experimental Mechanics* 46.3 (2006): 297-306.
[59] Liu, Zenghua, et al. "Temperature dependence of ultrasonic longitudinal guided wave propagation in long range steel strands." *Chinese Journal of Mechanical Engineering* 24 (2011): 1.
[60] Haag, Thomas, et al. "Wave-based defect detection and interwire friction modeling for overhead transmission lines." *Archive of Applied Mechanics* 79.6-7 (2009): 517-528.
[61] Branham, Stephanie L., et al. "Nondestructive testing of overhead transmission lines." *Conference on damage in composite materials, Stuttgart*. 2006.
[62] Gaul, Lothar, et al. "Structural health monitoring of cylindrical structures using guided ultrasonic waves." *Acta Mechanica* 223.8 (2012): 1669-1680.
[63] Baltazar, Arturo, Cesar D. Hernandez-Salazar, and Betsabe Manzanares-Martinez. "Study of wave propagation in a multiwire cable to determine structural damage." *NDT& E International* 43.8 (2010): 726-732.
[64] Mudge, P. J. "Field application of the Teletest long-range ultrasonic testing technique." *Insight* (2001).
[65] 2005 3-D Laser Vibrometer-User Manual (Germany: Polytec)
[66] Treyssède, Fabien, and Laurent Laguerre. "Investigation of elastic modes propagating in multi-wire helical waveguides." *Journal of sound and vibration*329.10 (2010): 1702-1716.
[67] Liu, Yijie, et al. "Numerical investigation of dispersion relations for helical waveguides using the Scaled Boundary Finite Element method." *Journal of Sound and Vibration* 333.7 (2014): 1991
[68] Alleyne, David N., and Peter Cawley. "A 2-dimensional Fourier transform method for the quantitative measurement of Lamb modes." *Ultrasonics Symposium, 1990. Proceedings., IEEE 1990*. IEEE, 1990.
[69] Hutchins, David, et al. "Coded waveforms for optimised air-coupled ultrasonic non-destructive evaluation." *Ultrasonics* (2014).
[70] Xu, Jiang, Hongfen Xiong, and Xinjun Wu. "Signal processing for the guided wave test based on the empirical mode decomposition." *Electrical and Control Engineering (ICECE), 2011 International Conference on*. IEEE, 2011.
[71] Marzani, A., et al. "High frequency guided waves in a 7 wire strand: Warped Frequency Transform for spectro-temporal characterization." *Ultrasonics Symposium (IUS), 2009 IEEE International*. IEEE, 2009.
[72] Zhang, Guang-Ming, and David M. Harvey. "Contemporary ultrasonic signal processing approaches for nondestructive evaluation of multilayered structures. " *Nondestructive Testing and Evaluation* 27.1 (2012): 1-27.
[73] Rizzo, Piervincenzo, and Francesco Lanza di Scalea. "Feature extraction for defect detection in strands by guided ultrasonic waves." *Structural Health Monitoring* 5.3 (2006): 297-308.
[74] Rizzo, Piervincenzo, and Francesco Lanza di Scalea. "Ultrasonic inspection of multi-wire steel strands with the aid of the wavelet transform." *Smart Materials and Structures* 14.4 (2005): 685.

[75] Hernandez-Salazar, C. D., Arturo Baltazar Herrejon, and J. I. Andara-Sanchez. "Damage detection in multi-wire cables using continuous wavelet transform analysis of ultrasonic guided waves." *Electronics, Robotics and Automotive Mechanics Conference, 2009. CERMA'09.*. IEEE, 2009.
[76] R.Sicard, J.Goyette, D.Zellouf, "A numerical dispersion compensation technique for time recompression of Lamb wave signals," Ultrasonics, vol. 40, no. 1-8, pp. 727-732, 2022.
[77] P. Wilcox, "A Rapid Signal Processing Technique to Remove the Effect of Dispersion from Guided Wave Signals," IEEE trans. on Ultrasonics, Ferroelectrics and Frequency Control, vol. 50, no. 4, pp. 419-427, 2003.
[78] T. Yamasaki , S. Tamai and M. Hirao , "Optimum excitation signal for long-range inspection of steel wires by longitudinal waves," NDT&E International, vol. 34, no. 3, pp. 207-212, 2001.
[79] K. Toiyama and T. Hayashi, "Pulse compression technique considering velocity dispersion of guided wave," in Review of Progress in Quantitative Non Destructive Evaluation: 34th Annual Review of Progress in Quantitative Nondestructive evaluation, 2008.
[80] L. De Marchi, A. Perelli, and A. Marzani, "A signal processing approach to exploit chirp excitation in Lamb wave defect detection and localization procedures," Mechanical Systems and Signal Processing, 2012.
[81] J.Lin, L.Zeng , "Chirp-based pre-compensation for high resolution Lamb wave inspection," NDT&E International, vol. 61, pp. 35-44, 2013.
[82] K. Xu, D. Ta, B. Hu, P. Laugier, and W. Wan, "Wideband dispersion reversal of lamb waves," IEEE Trans. on Ultrasonics, Ferroelectrics and Frequency Control, vol. 61, no. 6, pp. 997-1005, 2014.
[83] Donoho, David L., and Jain M. Johnstone. "Ideal spatial adaptation by wavelet shrinkage." *Biometrika* 81.3 (1994): 425-455.
[84] Pardo, E., et al. "Noise reduction in ultrasonic NDT using undecimated wavelet transforms." *Ultrasonics* 44 (2006): e1063-e1067.
[85]Zhang, Xiaohui, et al. "Flaw classification in ultrasonic guided waves signal using Wavelet Transform and PNN classifier." *Wireless Communications and Signal Processing (WCSP), 2011 International Conference on*. IEEE, 2011.
[86] COMSOL Inc., Last accessed Sep. 2014. COMSOL Multiphysics. http://www.comsol.com/.
[87]Wiens, T., 2009. Last accessed Sep. 2014. Kasami sequences, m-sequences, linear feedback shift registers. http://www.mathworks.com/matlabcentral/fileexchange/22716-kasami-sequences--m-sequences--linear-feedback-shift-registers/content/coding_1_02/kasami.m
[88] T. Misaridis and J.A. Jensen, "Use of Modulated Excitation Signals in Medical Ultrasound. Part 1: Basic Concepts and Expected Benefits," IEEE Trans. on Ultrasonic, Ferroelectrics and Frequency Control, vol. 52, no. 2, pp. 177-191, 2005.
[89] R. E Challis and V.G. Ivchenko, "Sub-threshold sampling in a correlation-based ultrasonic spectrometer," Measurement Science and Technology, vol. 22, no. 2, 2011.
[90] T.H. Gan, D.A. Hutchins, D.R. Billson and D.W. Schindel , "The use of broadband acoustic transducers and pulse-compression techniques for air-coupled ultrasonic imaging," Ultrasonics, pp. 181-194, 2011.
[91] T.H. Gan, D.A. Hutchins and R.J. Green, "Noncontact, high-resolution ultrasonic imaging of wood samples using coded chirp waveforms," IEEE Trans. on Ultrasonics, Ferroelectrics and Frequency Control, vol. 52, no. 2, pp. 280-288, 2005.

[92] M. Garcia-Rodriguez, Y. Yañez, M. J. Garcia-Hernandez, J. Salazar, A. Turo, and J. A. Chavez, "Application of Golay codes to improve the dynamic range in ultrasonic Lamb waves air-coupled systems," NDT&E International, vol. 43, no. 8, pp. 677-686, 2010.
[93] M. Ricci, L. Senni, P. Burrascano, R. Borgna, S. Neri, and M. Calderini, "Pulse-compression technique for the inspection of forged steel with high attenuation," Insight-Non Destructive Testing and Condition Monitoring, vol. 52, no. 2, pp. 91-95, 2012.
[94] M. Ricci, S. Callegari, S. Caporale, M. Monticelli, L. Battaglini, M. Eroli, L. Senni, R. Rovatti, G. Setti, and P. Burrascano, "Exploiting non-linear chirp and sparse deconvolution to enhance the performance of pulse-compression ultrasonic NDT," in IEEE International Ultrasonics Symposium (IUS), 2012.
[95] Z.Zhou, B. Ma, J. Jiang, G. Yu, K. Liu, D. Zhang, and W. Liu., "Application of wavelet filtering and Barker-coded pulse compression hybrid method to air-coupled ultrasonic testing," Nondestructive Testing and Evaluation, pp. 1-18, 2014.
[96] M. Ricci, L. Senni and P. Burrascano, "Virtual Instrument for air-coupled ultrasound NDT application based on Pseduo-Noise sequences," in International Workshop on ADC Modelling, Testing and Data Converter Analysis and Design, Orvieto,Italy, 2011.
[97] S.W. Golomb, Shift Register Sequences, Laguna Hills, CA: Aegean Park Press, 1982.
[98] T. J. Terrell and L.-K Shark, Digital Signal Processing, London: Macmillan Press, 1996.
[99] B. Engineer, "The Mechanical and Resonant Behaviour of a Dry Coupled Thickness-Shear PZT Transducer used for Guided Wave Testing in Pipe Line," PhD Thesis, School of Engineering and Design, Brunel University, London, 2013.

"…What we are trying to do, during all these discussions and talks here, is to see if we cannot radically bring about a transformation of the mind, not accept things as they are, nor revolt against them. Revolt doesn't answer a thing. You must understand it, go into it, examine it, give your heart and your mind, with everything that you have, to find out a way of living differently. That depends on you, and not on someone else, because in this there is no teacher, no pupil; there is no leader; there is no guru; there is no Master, no Savior. You yourself are the teacher and the pupil; you are the Master; you are the guru; you are the leader; you are everything. And to understand is to transform what is. "

J. Krishnamurti